



HAL
open science

Antarctic surface temperature and elevation during the Last Glacial Maximum

Christo Buizert, T. Fudge, William Roberts, Eric Steig, Sam Sherriff-Tadano,
Catherine Ritz, Eric Lefebvre, Jon Edwards, Kenji Kawamura, Ikumi Oyabu,
et al.

► **To cite this version:**

Christo Buizert, T. Fudge, William Roberts, Eric Steig, Sam Sherriff-Tadano, et al.. Antarctic surface temperature and elevation during the Last Glacial Maximum. *Science*, 2021, 372 (6546), pp.1097-1101. 10.1126/science.abd2897 . hal-03249154

HAL Id: hal-03249154

<https://hal.science/hal-03249154>

Submitted on 1 Jul 2021

HAL is a multi-disciplinary open access archive for the deposit and dissemination of scientific research documents, whether they are published or not. The documents may come from teaching and research institutions in France or abroad, or from public or private research centers.

L'archive ouverte pluridisciplinaire **HAL**, est destinée au dépôt et à la diffusion de documents scientifiques de niveau recherche, publiés ou non, émanant des établissements d'enseignement et de recherche français ou étrangers, des laboratoires publics ou privés.

1 **Antarctic surface temperature and elevation during the Last**

2 **Glacial Maximum**

3 **Authors:** Christo Buizert^{1*}, T.J. Fudge², William H. G. Roberts³, Eric J. Steig², Sam Sherriff-
4 Tadano⁴, Catherine Ritz⁵, Eric Lefebvre⁵, Jon Edwards¹, Kenji Kawamura⁶, Ikumi Oyabu⁶,
5 Hideaki Motoyama⁶, Emma C. Kahle², Tyler R. Jones⁷, Ayako Abe-Ouchi⁴, Takashi Obase⁴,
6 Carlos Martin⁸, Hugh Corr⁸, Jeffrey P. Severinghaus⁹, Ross Beaudette⁹, Jenna A. Epifanio¹,
7 Edward J. Brook¹, Kaden Martin¹, Jérôme Chappellaz¹⁰, Shuji Aoki¹¹, Takakiyo Nakazawa¹¹,
8 Todd A. Sowers¹², Richard B. Alley¹², Jinho Ahn¹³, Michael Sigl¹⁴, Mirko Severi¹⁵, Nelia W.
9 Dunbar¹⁶, Anders Svensson¹⁷, John Fegyveresi¹⁸, Chengfei He¹⁹, Zhengyu Liu¹⁹, Jiang Zhu²⁰,
10 Bette Otto-Bliesner²⁰, Vladimir Y. Lipenkov²¹, Masa Kageyama²², and Jakob Schwander¹⁴

11 ¹College of Earth Ocean and Atmospheric Sciences, Oregon State University, Corvallis OR
12 97331, USA

13 ²Department of Earth and Space Science, University of Washington, Seattle WA 98195, USA

14 ³Geographical and Environmental Sciences, Northumbria University, Newcastle, UK

15 ⁴Atmosphere and Ocean Research Institute, The University of Tokyo, Kashiwa 277-8568, Japan

16 ⁵Université Grenoble Alpes, CNRS, IRD, IGE, Grenoble, France

17 ⁶National Institute for Polar Research, Tachikawa, Tokyo, Japan

18 ⁷Institute of Arctic and Alpine Research, University of Colorado, Boulder CO 80309, USA

19 ⁸British Antarctic Survey, Cambridge, UK

20 ⁹Scripps Institution of Oceanography, University of California San Diego, La Jolla CA 92093 ,
21 USA

22 ¹⁰Univ. Grenoble Alpes, CNRS, IRD, Grenoble INP, IGE, 38000 Grenoble, France

23 ¹¹Center for Atmospheric and Oceanic Studies, Graduate School of Science, Tohoku University,
24 Sendai 980-8578, Japan

25 ¹²The Earth and Environmental Systems Institute, Pennsylvania State University, University
26 Park, PA 16802, USA

27 ¹³School of Earth and Environmental Sciences, Seoul National University, Seoul 08826, South
28 Korea

29 ¹⁴Climate and Environmental Physics, Physics Institute & Oeschger Center for Climate Change
30 Research, University of Bern, Sidlerstrasse 5, 3012 Bern, Switzerland

31 ¹⁵Department of Chemistry “Ugo Schiff”, University of Florence, Florence, Italy

32 ¹⁶New Mexico Bureau of Geology & Mineral Resources, Earth and Environmental Science
33 Department, New Mexico Tech, Socorro, NM 87801, USA

34 ¹⁷Niels Bohr Institute, University of Copenhagen, Copenhagen, Denmark

35 ¹⁸School of Earth and Sustainability, North Arizona University, Flagstaff, AZ 86011, USA

36 ¹⁹Department of Geography, Ohio State University, Columbus, OH 43210, USA

37 ²⁰National Center for Atmospheric Research, Boulder CO 80307, USA

38 ²¹Climate and Environmental Research Laboratory, Arctic and Antarctic Research Institute, St.
39 Petersburg, 199397, Russia

40 ²²Laboratoire des Sciences du Climat et de l’Environnement-IPSL, Université Paris-Saclay, Gif-
41 sur-Yvette, France

42 *Correspondence to: christo.buizert@oregonstate.edu

43

44

45 **Abstract:** Water stable isotopes in polar ice cores are a widely used temperature proxy in
46 paleoclimate reconstruction, yet calibration remains challenging in East Antarctica. Here we
47 reconstruct the magnitude and spatial pattern of Last Glacial Maximum surface cooling in
48 Antarctica using borehole thermometry and firn properties in seven ice cores. West Antarctic
49 sites cooled $\sim 10^{\circ}\text{C}$ relative to preindustrial. East Antarctic sites show a range from ~ 4 to $\sim 7^{\circ}\text{C}$
50 cooling, consistent with results of global climate models when the effects of topographic changes
51 indicated by ice-core air-content data are included, but less than indicated by use of water stable
52 isotopes calibrated against modern spatial gradients. An altered Antarctic temperature inversion
53 during the glacial reconciles our estimates with water isotope observations.

54 **One Sentence Summary:** Temperature reconstructions based on borehole thermometry and firn
55 properties, suggest that interpretation of ice core water isotopes using modern spatial slopes
56 overestimates last glacial maximum surface cooling in central East Antarctica.

57 **Main Text:**

58 Using oxygen and hydrogen isotope ratios in ancient polar ice as records of past site temperature
59 requires a calibration (1). Surface temperature and isotopic composition of precipitation correlate
60 spatially in Antarctica, with a regression coefficient α_s (spatial slope) of $0.80 \text{ } \text{‰K}^{-1}$ for $\delta^{18}\text{O}$ (2).
61 Reconstructing past temperatures requires regression over time, and this temporal slope α_T may
62 differ from α_s . In East Antarctica where the longest continuous ice core records, going back to 800
63 ka BP (thousands of years before present), have been extracted (3), independent temperature
64 estimates are not available and the spatial slope is commonly used to convert isotopic ratios to
65 temperature (1); this approach gives a surface temperature difference ΔT_s between the Last Glacial
66 Maximum (LGM, 26-18 ka BP) and preindustrial of around -9°C (1, 4, 5).

67 Antarctic LGM-preindustrial isotope changes depend on many factors including hemispheric sea-
68 surface temperatures (6), sea ice extent (7), ice sheet elevation (8), vapor origin and transport,
69 precipitation seasonality, and post-depositional isotopic exchange (9). Isotope-enabled general
70 circulation models seek to capture these physical processes, making them an invaluable tool for
71 studying isotopic variations. Such models simulate LGM-preindustrial α_T ranging from 0.3 to 1.4
72 ‰K⁻¹ in central East Antarctica (implied ΔT_s of 4 to 20°C), implying several aforementioned
73 processes are poorly constrained (8, 10-12).

74 We distinguish three temperatures: (i) the climatic temperature T_{CLIM} at constant elevation (relative
75 to the present-day geoid); (ii) the surface temperature T_s , which may differ from the climatic
76 temperature due to changing ice sheet topography; and (iii) the vapor condensation temperature
77 T_c , which is warmer than the surface due to the strong Antarctic inversion (2, 13).

78 Here, we empirically reconstruct LGM surface temperature across Antarctica (Fig. 1) using two
79 independent methods. We investigate five East Antarctic ice cores: EPICA (European Project for
80 Ice Coring in Antarctica) Dome C (EDC), EPICA Dronning Maud Land (EDML), Dome Fuji
81 (DF), Talos Dome (TAL), and South Pole (SP); and two West Antarctic cores: West Antarctic Ice
82 Sheet (WAIS) Divide (WD), and Siple Dome (SDM).

83 First, we estimate ΔT_s at EDC and DF from the measured borehole temperature profiles (Fig. 2)
84 using a method similar to that employed recently at WD (14). Due to the downward ice flow and
85 low thermal diffusivity, the ice sheet maintains an imprint of its past surface temperature history.
86 The large ice sheet thickness at EDC and DF is favorable for preserving past temperatures, yet the
87 low accumulation rate is not. Consequently, the relative uncertainty in the EDC and DF borehole
88 reconstructions is larger than that at WD. To constrain the problem better we use downward ice

89 velocities measured via phase-sensitive radio echo sounding (EDC only), and accurate age
90 constraints derived via volcanic synchronization to the layer-counted WD timescale.

91 We force a 1-D heat transport-ice flow model at the surface boundary with a temperature history
92 based on the $\delta^{18}\text{O}$ record scaled with a constant α_T value (10). Applying traditional isotope scaling
93 ($\alpha_T \approx 0.7 \text{ ‰ K}^{-1}$, yielding $\Delta T_s = -9^\circ\text{C}$ at EDC and -7.5°C at DF) simulates temperature profiles that
94 do not fit the borehole observations at either site (Fig. 2). At EDC the model-data fit is optimized
95 for $\alpha_T = 1.14 \text{ ‰ K}^{-1}$ consistent with $\Delta T_s = -5.5^\circ\text{C}$ (95% confidence range is -6.9°C to -3.1°C). At
96 DF the optimal ΔT_s is in the -2.0°C to -5.4°C range; we provide a range without a best estimate
97 because at DF there are no direct constraints on the downward ice velocity. In Fig. 1 the WD, EDC
98 and DF borehole estimates are marked “BH”.

99 Second, we reconstruct past climate at all seven sites using the dependence of firn densification,
100 the gradual transformation of polar snow to ice, on T_s and accumulation rate (A). Air bubbles are
101 isolated from the atmosphere at the lock-in depth (50-120 m below the surface), an event preserved
102 in two ice core signals (15): $\delta^{15}\text{N}$ of N_2 which records past firn column thickness via gravitational
103 enrichment, and the gas age-ice age difference or Δage . Critically, the $\delta^{15}\text{N}$ and Δage -isopleths are
104 perpendicular in T_s - A space (Fig. 3A), meaning that if $\delta^{15}\text{N}$ and Δage are independently known, a
105 unique climatic [T_s , A] solution exists (subject to the uncertainties of the firn model).

106 Synchronization using both volcanic deposits and globally synchronous abrupt atmospheric
107 methane variations, allows us to estimate Δage empirically for the Antarctic ice cores (10, 16). We
108 use an inverse dynamical firn densification-heat transport model (17, 18) to reconstruct T_s and A
109 histories that optimize the fit to Δage and $\delta^{15}\text{N}$ data (Fig. 3B-C). Reconstructed accumulation rates
110 agree (within uncertainty) with independent estimates (Fig. S8). Methodological biases and

111 uncertainties are estimated using a Monte-Carlo approach (10). The histograms in Fig.1 give the
112 ΔT_s distribution of the Δage -based reconstruction.

113 In East Antarctica, ΔT_s ranges from $-3.8 \pm 2.0^\circ\text{C}$ (DF) to $-7.1 \pm 1.7^\circ\text{C}$ (TAL); at DF, EDC and EDML,
114 ΔT_s is substantially lower than estimates from isotope scaling using α_s . The two West Antarctic
115 sites have similar ΔT_s of $-10.2 \pm 2.4^\circ\text{C}$ (SDM) to $-10.3 \pm 1.3^\circ\text{C}$ (WD). The Δage - and borehole-based
116 reconstruction methods agree within uncertainty at all sites (Fig. 1). Allowing for more flank-like
117 ice flow at EDC during the glacial period (which would occur if the divide position were different
118 than at present), improves the agreement by changing the borehole estimate to around -4.5°C (10);
119 we choose to report the -5.5°C value to keep both methods independent. PMIP4 (Paleoclimate
120 Modeling Intercomparison Project phase 4) simulations (19) find a seven-site-mean ΔT_s
121 magnitude that is $1.2 \pm 4.6^\circ\text{C}$ larger than our Δage -based reconstructions (mean and spread of ten
122 climate models; Fig. 1).

123 We emphasize that the firm method is primarily constrained by the empirical Δage estimates.
124 Because T_s and A broadly co-vary via the saturation vapor pressure, the deglacial climatic changes
125 run parallel to the $\delta^{15}\text{N}$ -isopleths (Fig. 3A). Therefore, $\delta^{15}\text{N}$ data alone do not constrain the
126 magnitude of climate change meaningfully. The effects of T_s and A are additive in Δage , however,
127 making Δage a sensitive proxy for climate change (Fig. 3D), as first noted by Jakob Schwander
128 (20). The empirical Δage at 24ka is larger than at 18 ka BP for all five cores where both are
129 available, and coldest conditions in Antarctica occur around 27-24 ka BP in our reconstructions
130 (Fig. S8h); this follows expectations from local insolation (21).

131 We propose that elevation changes explain the spatial differences in ΔT_s (8). Let Δz be the LGM
132 elevation anomaly relative to present. We present new WD and DF total air content data (Fig.
133 S12), and interpret them in terms of elevation change (22). These data suggest a 420 m (range: 280
134 – 590 m) contrast in Δz between WD and central East Antarctica (here DF and EDC) – for example
135 $\Delta z = +300$ m at WAIS and $\Delta z = -120$ m in central East Antarctica (Fig. 4B). Our estimate is broadly
136 in agreement with LGM ice sheet reconstructions that suggest a West-East Δz contrast between
137 160 and 560 m (10). Although the implied Δz at WAIS exceeds the observed highstand at ice
138 margin nunataks (23), such data do not strongly constrain the elevation at WD over 500 km away.
139 The corresponding ΔT_s contrast (WD ΔT_s minus the average ΔT_s at DF and EDC) is $-6.2 \pm 2.3^\circ\text{C}$
140 in the Δ age-based reconstructions, $-6.0 \pm 2.0^\circ\text{C}$ in the borehole reconstructions, and $-5.9 \pm 2.7^\circ\text{C}$
141 in the PMIP4 model ensemble; the level of agreement suggests this is a robust feature of Antarctic
142 LGM climate. This temperature contrast is thus plausibly linked to Δz via the (spatial) lapse rate
143 in interior of Antarctica of around $-12^\circ\text{C km}^{-1}$ (2, 24).

144 To further assess the elevation impact on ΔT_s we perform an atmosphere-ocean general circulation
145 model (AOGCM) sensitivity study of Antarctic LGM climate using the MIROC and HadCM3
146 models and a series of LGM topographic reconstructions (10). We first estimate climatic LGM
147 cooling using full LGM boundary conditions (including LGM albedo) but preindustrial Antarctic
148 topography; this yields a seven-site average ΔT_{CLIM} of -4.7°C and -7.0°C in the MIROC and
149 HadCM3 models respectively, but stronger albedo-driven cooling is found over the Ross and
150 Weddell Seas due to ice growth onto the continental shelf (Fig. 4A). Note that simulated climatic
151 ΔT_{CLIM} is similar in interior West and East Antarctica in the absence of topographic change.

152 Next, we perform climate simulations with five Antarctic LGM topographic reconstructions. These
153 reconstructions suggest Δz of +100 to +600 m in interior WAIS and down to -250 m in interior
154 East Antarctica (Fig. 4B). These changes result in greater ΔT_s in West than in central East
155 Antarctica (Fig. 4C), in agreement with our reconstructions. By comparing the various topographic
156 reconstructions, we find that ΔT_s is closely linked to Δz in both models following the dry adiabatic
157 lapse rate of $-9.8^\circ\text{C km}^{-1}$ (Fig. 4D). There is also a fraction of the variance that cannot be explained
158 by lapse rate effects that is due to the topography altering the atmospheric circulation around
159 Antarctica. We find a correlation $r = 0.96$ between the reconstructed and the simulated site ΔT_s
160 pattern (averaged across the five topographic reconstructions and both models); for the PMIP4
161 multi-model mean this correlation is $r = 0.95$. We conclude that LGM ice sheet topography change
162 plausibly explains the ΔT_s spatial variability in our reconstruction (8).

163 Our findings have implications for the interpretation of water isotopes in Antarctic ice cores. We
164 find α_T in the range of 0.9 to 1.4 ‰K^{-1} in East Antarctica and therefore $\alpha_T > \alpha_S$, opposite to
165 Greenland where $\alpha_T < \alpha_S$ (17, 25). We compare our α_T with those from LGM and preindustrial
166 simulations using the latest generation isotope-enabled Community Earth System Model (iCESM,
167 Fig. 4E). The good agreement ($r = 0.91$; 0.06 ‰K^{-1} mean offset) demonstrates our reconstructed
168 α_T are consistent with isotope physics, yet the large inter-model spread in simulated α_T (see section
169 S3.5 in (10) for a review) prevents us from claiming it validates our results. While the α_T agree
170 well, iCESM simulates a ΔT_s and LGM-preindustrial $\delta^{18}\text{O}$ change that are both too large
171 (compared to our reconstructions and ice core data, respectively).

172 Last, we investigate changes to the strong surface-based inversion in the Antarctic boundary layer
173 (Fig. 4F). The condensation temperature T_C is higher than T_s , and they correlate spatially with a

174 slope dT_C/dT_S in the 0.63-0.67 range (2, 13, 26). T_C controls precipitation $\delta^{18}\text{O}$, with a present-day
175 spatial sensitivity of $d\delta^{18}\text{O}/dT_C = d\delta^{18}\text{O}/dT_S \times dT_S/dT_C \approx 0.80/0.65 = 1.23 \text{ ‰ K}^{-1}$. We now assume
176 that, unlike ΔT_S , the LGM-preindustrial change ΔT_C can be estimated using this spatial slope via
177 $\Delta T_C = \Delta\delta^{18}\text{O}/1.23$ (Fig. 4F). At WD and SDM the $\alpha_T \approx \alpha_S$ assumption holds, suggesting the ratio
178 $\Delta T_C/\Delta T_S$ is close to the present-day ratio of 0.65; in central East Antarctica the ratio $\Delta T_C/\Delta T_S$
179 exceeds 0.65 consistent with $\alpha_T > \alpha_S$. We plotted simulated ΔT_S vs. ΔT_C across interior Antarctica
180 from a wide range of AOGCMs and topographies; we find the ratio $\Delta T_C/\Delta T_S$ ranges from 0.48 to
181 1.3 (95% interval, grey lines) with our empirical reconstructions falling within the model data
182 cloud (Fig. 4F). In aggregate these simulations find that $\Delta T_C/\Delta T_S$ tends to exceed the present-day
183 ratio of 0.65 (~79% of model data points) – such a change to the inversion structure would result
184 in $\alpha_T > \alpha_S$ for ΔT_S . In the iCESM simulations the $\Delta T_C/\Delta T_S$ and α_T fields look similar, with the
185 $\Delta T_C/\Delta T_S = 0.65$ contour line broadly aligning with the $\alpha_T = 0.8 \text{ ‰K}^{-1}$ contour line (Fig. S11). We
186 conclude that physically plausible changes to the inversion (27, 28) may reconcile our
187 reconstructions with previous work on Antarctic LGM water isotopes.

188 Our reconstructions improve the LGM Antarctic temperature estimation and provide a benchmark
189 for testing the ability of (isotope-enabled) climate models to simulate climate states radically
190 different from the late Holocene. For surface temperature, the spatial isotopic slope is not always
191 a good approximation of the temporal slope, challenging the prevalent interpretation of ice core
192 water isotopes in Antarctica.

193

- 195 1. J. Jouzel *et al.*, Magnitude of isotope/temperature scaling for interpretation of central Antarctic ice cores. *J. Geophys. Res.* **108**, 4361 (2003).
- 196 2. V. Masson-Delmotte *et al.*, A Review of Antarctic Surface Snow Isotopic Composition: Observations, Atmospheric Circulation, and Isotopic Modeling. *J. Clim.* **21**, 3359-3387 (2008).
- 197 3. EPICA-Community-Members, Eight glacial cycles from an Antarctic ice core. *Nature* **429**, 623-628
- 198 (2004).
- 199 4. V. Masson-Delmotte *et al.*, EPICA Dome C record of glacial and interglacial intensities. *Quat. Sci. Rev.* **29**,
- 200 113-128 (2010).
- 201 5. J. Jouzel *et al.*, Orbital and millennial Antarctic climate variability over the past 800,000 years. *Science*
- 202 **317**, 793-796 (2007).
- 203 6. C. Risi, S. Bony, F. Vimeux, J. Jouzel, Water-stable isotopes in the LMDZ4 general circulation model:
- 204 Model evaluation for present-day and past climates and applications to climatic interpretations of tropical
- 205 isotopic records. *J. Geophys. Res.* **115**, (2010).
- 206 7. D. Noone, I. Simmonds, Sea ice control of water isotope transport to Antarctica and implications for ice
- 207 core interpretation. *Journal of Geophysical Research: Atmospheres (1984–2012)* **109**, (2004).
- 208 8. M. Werner, J. Jouzel, V. Masson-Delmotte, G. Lohmann, Reconciling glacial Antarctic water stable
- 209 isotopes with ice sheet topography and the isotopic paleothermometer. *Nature Communications* **9**, 3537
- 210 (2018).
- 211 9. M. Casado *et al.*, Archival of the water stable isotope signal in East Antarctic ice cores. *The Cryosphere*
- 212 *Discuss.* **2016**, 1-33 (2016).
- 213 10. Materials and methods are available as supplementary materials on Science Online.
- 214 11. J.-E. Lee, I. Fung, D. J. DePaolo, B. Otto-Bliesner, Water isotopes during the Last Glacial Maximum: New
- 215 general circulation model calculations. *J. Geophys. Res.* **113**, (2008).
- 216 12. G. Hoffmann, J. Jouzel, V. Masson, Stable water isotopes in atmospheric general circulation models.
- 217 *Hydrological Processes* **14**, 1385-1406 (2000).
- 218 13. J. Jouzel, L. Merlivat, Deuterium and oxygen 18 in precipitation: Modeling of the isotopic effects during
- 219 snow formation. *J. Geophys. Res.* **89**, 11749-11757 (1984).
- 220 14. K. M. Cuffey *et al.*, Deglacial temperature history of West Antarctica. *Proc. Natl. Acad. Sci. U. S. A.*,
- 221 (2016).
- 222 15. T. Sowers, M. Bender, D. Raynaud, Y. S. Korotkevich, $\delta^{15}\text{N}$ of N_2 in air trapped in polar ice: A tracer of
- 223 gas transport in the firn and a possible constraint on ice age-gas age differences. *J. Geophys. Res.* **97**,
- 224 15683-15697 (1992).
- 225 16. J. A. Epifanio *et al.*, The SP19 chronology for the South Pole Ice Core - Part 2: gas chronology, delta age,
- 226 and smoothing of atmospheric records. *Clim. Past* **2020**, 2431–2444 (2020).
- 227 17. C. Buizert *et al.*, Greenland temperature response to climate forcing during the last deglaciation. *Science*
- 228 **345**, 1177-1180 (2014).
- 229 18. M. M. Herron, C. C. Langway, Firn densification: An empirical model. *J. Glaciol.* **25**, 373-385 (1980).
- 230 19. M. Kageyama *et al.*, The PMIP4 contribution to CMIP6-Part 4: Scientific objectives and experimental
- 231 design of the PMIP4-CMIP6 Last Glacial Maximum experiments and PMIP4 sensitivity experiments.
- 232 *Geoscientific Model Development* **10**, 4035-4055 (2017).
- 233 20. J. Schwander *et al.*, Age scale of the air in the summit ice: Implication for glacial-interglacial temperature
- 234 change. *J. Geophys. Res.* **102**, 19483-19493 (1997).
- 235 21. P. Huybers, G. Denton, Antarctic temperature at orbital timescales controlled by local summer duration.
- 236 *Nature Geosci* **1**, 787-792 (2008).
- 237 22. D. Raynaud *et al.*, The local insolation signature of air content in Antarctic ice. A new step toward an
- 238 absolute dating of ice records. *Earth Planet. Sci. Lett.* **261**, 337-349 (2007).
- 239 23. P. Spector, J. Stone, B. Goehring, Thickness of the divide and flank of the West Antarctic Ice Sheet
- 240 through the last deglaciation. *The Cryosphere* **13**, 3061-3075 (2019).
- 241 24. J. Fortuin, J. Oerlemans, Parameterization of the annual surface temperature and mass balance of
- 242 Antarctica. *Ann. Glaciol* **14**, 78-84 (1990).
- 243 25. K. M. Cuffey *et al.*, Large Arctic Temperature Change at the Wisconsin-Holocene Glacial Transition.
- 244 *Science* **270**, 455-458 (1995).
- 245
- 246

- 247 26. W. Connolley, The Antarctic temperature inversion. *International Journal of Climatology: A Journal of the*
248 *Royal Meteorological Society* **16**, 1333-1342 (1996).
- 249 27. G. Krinner, C. Genthon, GCM simulations of the Last Glacial Maximum surface climate of Greenland and
250 Antarctica. *Clim. Dyn.* **14**, 741-758 (1998).
- 251 28. N. P. Van Lipzig, E. Van Meijgaard, J. Oerlemans, The effect of temporal variations in the surface mass
252 balance and temperature-inversion strength on the interpretation of ice-core signals. *J. Glaciol.* **48**, 611-621
253 (2002).
- 254 29. L. Tarasov, A. S. Dyke, R. M. Neal, W. R. Peltier, A data-calibrated distribution of deglacial chronologies
255 for the North American ice complex from glaciological modeling. *Earth Planet. Sci. Lett.* **315–316**, 30-40
256 (2012).
- 257 30. C. Buizert *et al.*, The WAIS Divide deep ice core WD2014 chronology - part 1: Methane synchronization
258 (68-31 ka BP) and the gas age-ice age difference. *Climate of the Past* **11**, 153-173 (2015).
- 259 31. M. Sigl *et al.*, The WAIS Divide deep ice core WD2014 chronology – Part 2: Annual-layer counting (0–
260 31 ka BP). *Clim. Past* **12**, 769-786 (2016).

261

262 **Acknowledgments:** The idea of weak East Antarctic LGM cooling was suggested a decade ago
263 by Sigfús J. Johnsen (1940–2013) and Jakob Schwander, but never published. We thank Emilie
264 Capron and Amaëlle Landais for help in gathering $\delta^{15}\text{N}$ data; Takeo Hondoh and Takao Kameda
265 for support in Dome Fuji air content analyses; Camille Bréant for sharing model output; Vasileios
266 Gkinis for useful discussions; Wing-Le Chan for assistance with model analysis; Jean-Yves
267 Peterschmitt for compiling PMIP4 model data, and all PMIP4 groups for sharing model output;
268 Chris Adams of Corvidopolis for providing a toddler-free workspace during the COVID-19
269 pandemic.

270 **Funding:** This work was supported by the US National Science Foundation (NSF) through grants
271 1643394 (to C.B.), 1643355 (to T.J.F. and E.J.S), 1443472, 1643722 (to E.J.B), and 1738934 (to
272 R.B.A.); the University of Washington Royalty Research Fund (to T.J.F); MEXT and the Japan
273 Society for the Promotion of Science KAKENHI Grant Numbers 18749002, 26241011,
274 15KK0027, 17H06316 and 20H00639 (to K.K), 20H04327 (to I.O.), 22310003 (to T.N.),
275 15J12515, 17H06104, 17H06323 and 20K14552 (to A.A-O); the National Research Foundation
276 of Korea (NRF) through grants NRF-2018R1A2B3003256 and NRF-2018R1A5A1024958 (to

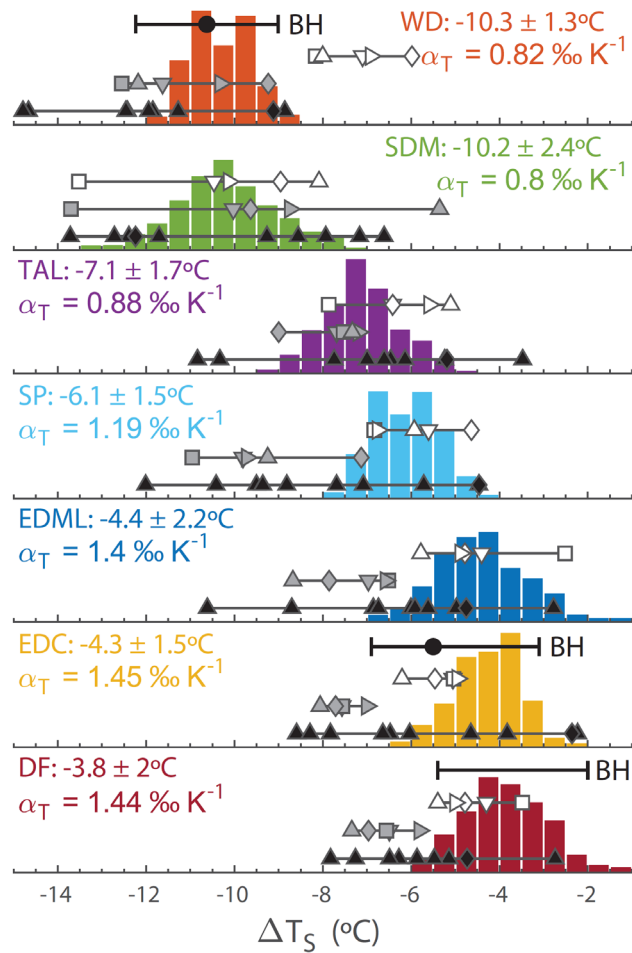
277 J.A.); the European Research Council (ERC) under the European Union's Horizon 2020 research
278 and innovation programme through grant agreement No 820047 (to M.Si.); IT-MIUR-PNRA
279 (Italian Antarctic Research Program) through the BE-OI (PNRA16_00124) project (to M.Se.); the
280 Villum Investigator Project IceFlow (NR. 16572, to A.S.); Beyond EPICA - Oldest Ice Core EU
281 Coordination and Support Action; measurements at EDC (Concordia Station) were supported by
282 the French Polar Institute (IPEV, prog 902) and the Italian Antarctic Program (PNRA and ENEA).

283 **Author Contributions:** C.B., E.J.S., and W.H.G.R. conceived of the study; Δ age-based
284 reconstructions by C.B.; ice flow and borehole temperature modeling by T.J.F. and C.R.; GCM
285 modeling by W.H.G.R., S.S.-T., T.O., A.A.-O., C.H., Z.L., J.Z., and B.O.-B.; PMIP4 model
286 compilation by M.K.; methane data by E.J.B., J.E., J.A., K.M., J.C., T.A.S., K.K., S.A. and T.N.;
287 $\delta^{15}\text{N-N}_2$ data by I.O., K.K., R.B., J.P.S., S.A. and T.N.; borehole thermometry data by C.R., E.L.
288 and H.M.; ApRES data by C.M. and H.C.; SP isotope data by E.J.S., E.C.K. and T.R.J.; air content
289 data and corrections by J.E., K.K., V.L., J.F. and R.B.A.; SDM chronology by T.J.F. and C.B.;
290 SDM tephra matches by N.W.D.; volcanic matching by M.Si., M.Se., A.S., T.J.F. and C.B.; J.Sc.
291 (and S.J.J.) independently performed a similar study that reached the same conclusion around a
292 decade ago; all authors contributed towards the final manuscript.

293 **Competing interests:** The authors declare no competing financial interests.

294 **Data and materials availability:** All new ice core data from this study are available in the
295 supplementary material data sheet and online at <https://www.ncdc.noaa.gov/paleo/study/32632>;
296 previously published data are available with their original publications and/or in publicly
297 accessible online data archives.

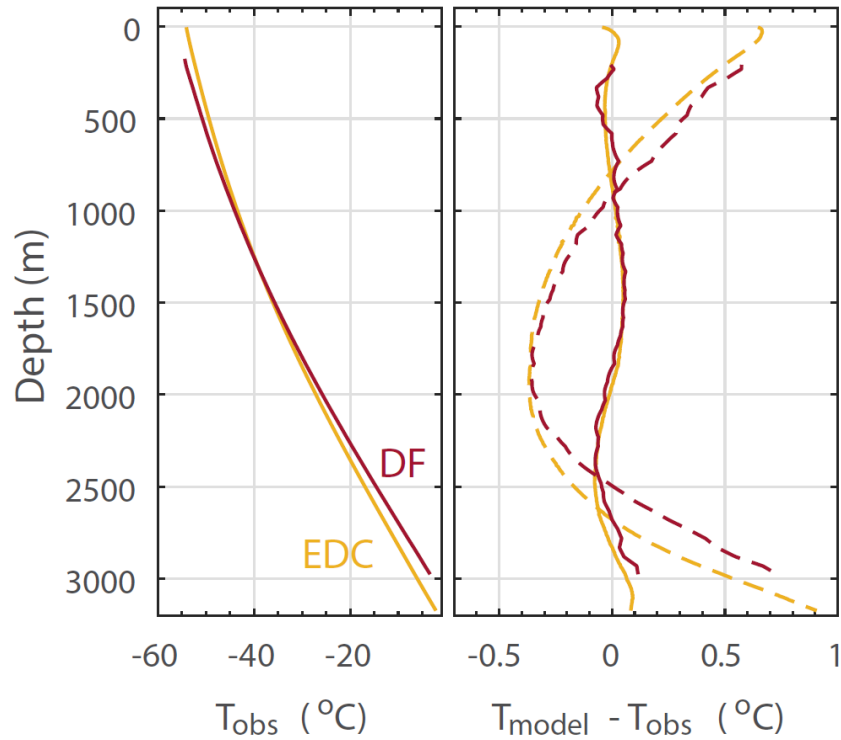
298



299

300 **Figure 1. Summary of Antarctic LGM cooling estimates.** Black markers with horizontal
 301 errorbars marked “BH” give borehole estimates; WD results from ref. (14). Histograms give
 302 distribution of Δ age-based temperature reconstructions from a Monte Carlo sampling ($N = 1000$)
 303 of model parameters; listed are mean and 2σ standard deviation of the distribution, as well as the
 304 implied temporal isotope slope α_T . ΔT_S is the LGM (18-21.4 ka BP) minus preindustrial (0.5-2.5
 305 ka BP) condition. White (MIROC), grey (HadCM3) and black (PMIP4) show AOGCM-simulated
 306 ΔT_S , with symbols denoting different LGM topography reconstructions (10): Pollard and Deconto
 307 2009 (downward triangle); Whitehouse et al. 2012 (square); Glac-1D (diamond, (29)); Golledge
 308 et al. 2014 (rightward triangle); Ice-6G (upward triangle).

309

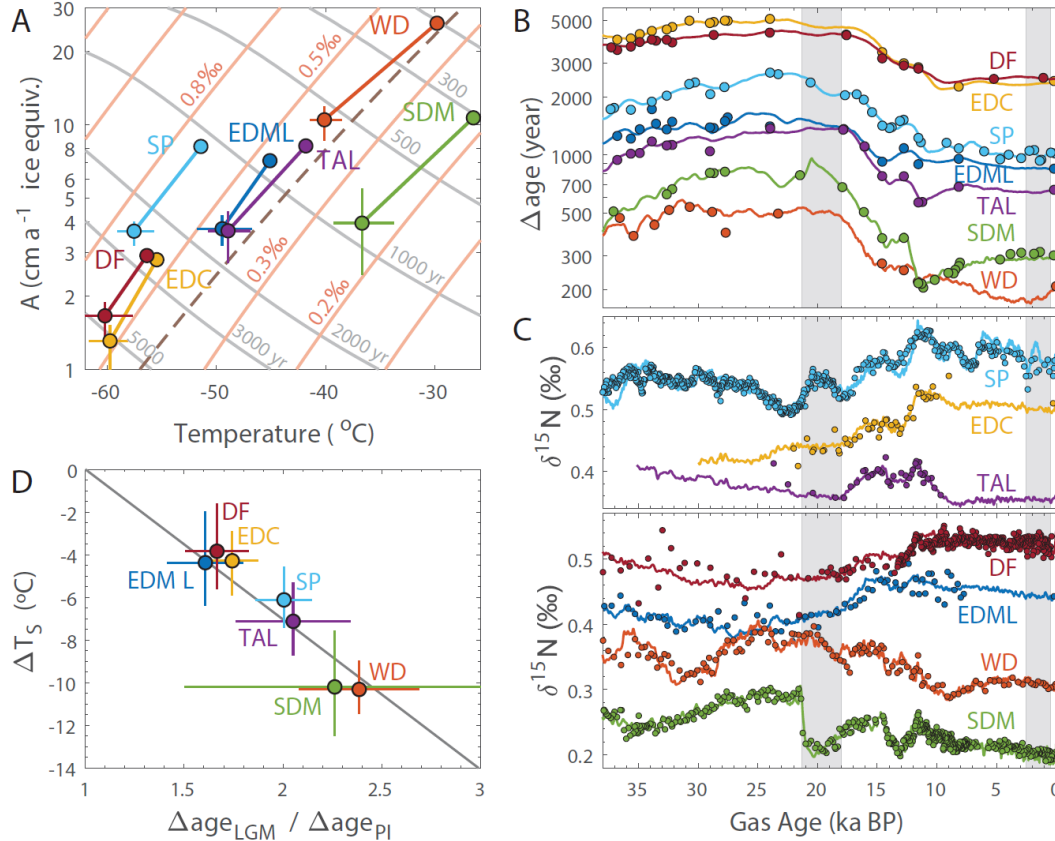


310

311 **Figure 2. Borehole temperature reconstruction for EDC and DF.** Left panel: Site borehole
 312 temperature observations at EDC (yellow) and DF (red). At both sites the ice-bedrock interface is
 313 at the pressure melting point (-2.2°C). Right panel: model-data mismatch at EDC (yellow) and DF
 314 (red) for an ice flow-heat transport model forced by the optimized temperature histories (solid
 315 lines, ΔT_s of -5.5°C at EDC and -3.2°C at DF), and forced with water-isotope scaling of 0.7‰K^{-1}
 316 ¹ (dashed lines, ΔT_s of -9.0°C at EDC and -7.5°C at DF).

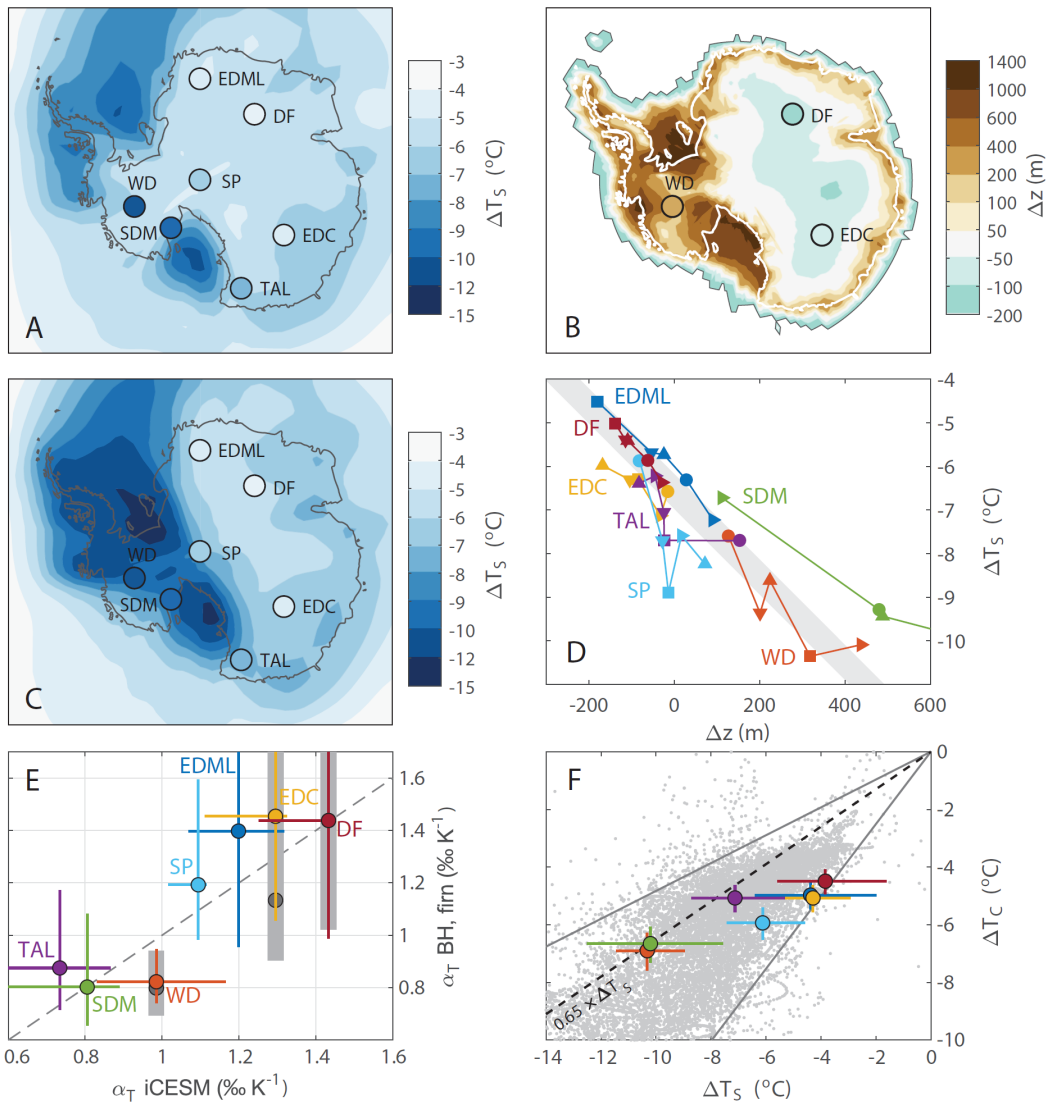
317

318



319

320 **Figure 3. Δ age-based temperature reconstructions.** (A) Δ age and $\delta^{15}\text{N}$ -isopleths (grey and
 321 salmon, respectively) in the steady-state Herron-Langway firn densification model as a function
 322 of T_s and A . Dashed line shows accumulation scaling via the saturation vapor pressure at the site
 323 (ignoring the atmospheric inversion). Reconstructed preindustrial and LGM conditions at the
 324 seven sites are indicated. (B) Model fit to empirical Δ age constraints. Grey vertical bars denote the
 325 LGM (21.4-18 ka BP) and preindustrial (2.5-0.5 ka BP) periods. (C) Model fit to $\delta^{15}\text{N}$ data, divided
 326 over two panels to prevent overlapping curves. Data shown on the WD2014 timescale (30, 31).
 327 (D) Reconstructed ΔT_s versus ratio of LGM Δ age over preindustrial Δ age (with linear fit), showing
 328 the utility of Δ age as a climate proxy.



329

330 **Figure 4. Climate models and Antarctic topography.** (A) AOGCM simulations of ΔT_s using
 331 preindustrial ice topography in Antarctica (average of MIROC and HadCM models), with Δ age-
 332 based ΔT_s reconstructions for the seven sites. (B) simulated LGM elevation anomaly (shaded,
 333 average of five topographies) with LGM elevation anomaly of +310 m, -80 m, and -140 m at WD,
 334 EDC and DF (10) (C) As in panel (A), but using LGM ice topography in Antarctica (average of
 335 five LGM topographies and both MIROC and HadCM models). (D) Elevation change vs. ΔT_s in
 336 the AOGCM simulations (average of MIROC and HadCM models); symbols denote the different

337 LGM topographic reconstructions (see Fig. 1 caption for legend). The grey bar shows the dry
338 adiabatic lapse rate. **(E)** Temporal isotope slope α_T from the iCESM model against our
339 reconstructions (borehole in grey, Δ age-based in colors). **(F)** ΔT_s vs ΔT_C from Δ age-based ΔT_s and
340 isotope-based ΔT_C (large dots with error bars) and from LGM-preindustrial AOGCM simulations
341 (small grey dots, grey lines enclose the central 95% of estimates); black dashed line gives modern
342 spatial slope (2). Models plotted are PMIP3 (except CNRM-CM5 that simulates $\Delta T_s > 0^\circ\text{C}$),
343 PMIP4 (all model output publicly available), and all iCESM, MIROC and HadCM3 simulations
344 used in this work; we show interior Antarctica (surface pressure > 800 hPa); T_C is taken to be the
345 annual mean troposphere temperature maximum (typically around 500hPa). The models have an
346 average preindustrial spatial dT_C/dT_s of 0.68 (range: 0.31 to 0.89) in interior Antarctica.

347

348 **Content of the Supplementary Materials:**

349 Materials and Methods

350 Figures S1 to S12

351 Tables S1 to S7

352 References 32-154 are only called out in the supplementary materials.

353

Science



1
2
3
4
5
6
7
8
9
10
11
12
13
14
15
16
17
18
19
20
21
22
23
24
25

Supplementary Materials for

Antarctic surface temperature and elevation during the Last Glacial Maximum

Christo Buizert*, T.J. Fudge, William H. G. Roberts, Eric J. Steig, Sam Sherriff-Tadano, Catherine Ritz, Eric Lefebvre, Jon Edwards, Kenji Kawamura, Ikumi Oyabu, Hideaki Motoyama, Emma C. Kahle, Tyler R. Jones, Ayako Abe-Ouchi, Takashi Obase, Carlos Martin, Hugh Corr, Jeffrey P. Severinghaus, Ross Beaudette, Jenna Epifanio, Edward J. Brook, Kaden Martin, Jérôme Chappellaz, Shuji Aoki, Takakiyo Nakazawa, Todd A. Sowers, Richard Alley, Jinho Ahn, Michael Sigl, Mirko Severi, Nelia W. Dunbar, Anders Svensson, John Fegyveresi, Chengfei He, Zhengyu Liu, Jiang Zhu, Bette Otto-Bliesner, Vladimir Y. Lipenkov, Masa Kageyama, and Jakob Schwander

*Correspondence to: christo.buizert@oregonstate.edu

This PDF file includes:

- Materials and Methods
- Figures S1 to S12
- Tables S1 to S7
- Additional References 32-154

Other Supplementary Material for this manuscript includes the following:

- Data Excel file S1

26 **Materials and Methods**

27

28 **S1 Borehole temperature reconstructions at Dome C and Dome F**

29 **S1.1 Models and data**

30 **S1.1.1 Forward ice flow-heat transport model**

31 We use a transient one-dimensional ice-flow model to compute the vertical-velocity profile through time:

$$32 \quad w(\hat{z}) = -(\dot{b} - \dot{m} - \dot{H})\psi(\hat{z}) - \dot{m} - \left(\frac{\rho_{ice}}{\rho_{firm}} - 1\right)\dot{b} \quad (S1)$$

33 where \hat{z} is the non-dimensional height above the bed, \dot{b} is the accumulation rate, \dot{m} is the melt rate, \dot{H} is
34 the rate of ice-thickness change, ρ_i is the density of ice, ρ_{firm} is the density profile and $\psi(\hat{z})$ is the vertical
35 velocity shape function computed as:

$$36 \quad \psi(\hat{z}) = \left(1 - \frac{p+2}{p+1}(1 - \hat{z}) + \frac{1}{p+1}(1 - \hat{z})^{p+2}\right) \quad (S2)$$

37 following Lliboutry (1979) where p is vertical velocity shape parameter (32). Firm compaction is
38 incorporated through the right hand term in equation S1 and assumes a density profile that does not vary
39 with time.

40 The heat equation following Cuffey and Paterson (2010) is (33):

$$41 \quad \rho c_p \frac{\partial T}{\partial t} = \frac{\partial}{\partial z} \left(k \frac{\partial T}{\partial z} \right) - \rho c_p w \frac{\partial T}{\partial z} + Q \quad (S3)$$

42 where c_p is the heat capacity, T is temperature, k is the thermal conductivity, and Q is the heat production
43 term, and z is the height above the bed. The firm density profile is modeled using the Herron and Langway
44 model (18) matched to modern measurements to assure a smooth vertical velocity profile. Values of c_p are
45 temperature dependent and calculated at each time step using the relationships from ref. (34). For k , we use
46 three different relationships as described below (Section S1.2.1). The thermal conductivity in the firm is
47 found using the relationship in ref. (35).

48 **S1.1.2 Borehole temperature measurements**

49 The EDC borehole temperature measurements were made in 2008 to a depth of 3235 m where the probe
50 could no longer descend, possibly due to partial borehole closure. The temperature was extended to the
51 pressure melting temperature of -2.18°C at the ice-rock interface at 3275 m. The principle of the probe is a
52 four-wires circuit to measure the resistance of the temperature sensor (36). The upper 100 m of
53 measurements are less reliable because they were made in the cased portion of the firm and have been
54 excluded from our analysis. The data have been smoothed with a 5 m Hanning window. The uncertainty of
55 the temperature measurements is 1 cK. The temperature profile is shown in Fig. 1 of the main text.

56 The Dome Fuji borehole temperature measurements were made in January 2013 on the DF-2 borehole using
57 a Pt-100 resistance thermometer. As at EDC, the upper 100 m of measurements are less reliable because
58 they were made in the cased portion of the firm and have been excluded from our analysis. The data are
59 averaged over 50 m intervals to improve the signal-to-noise ratio. The uncertainty of the temperature
60 measurements is 5 cK. The temperature profile is shown in Fig. 2 of the main text.

61 **S1.1.3 Vertical velocity measurement**

62 Phase sensitive radar measurements (ApRES) allow the determination of englacial vertical velocities (37).
63 Three sets of measurements have been made with one year repeat intervals at Dome C. We focus on the
64 highest quality measurements made in 2016 and 2017 (Figure S1). We use the ApRES measurements to
65 constrain the Lliboutry p parameter by finding the best fit where the surface vertical velocity is also a free
66 parameter (38). We do not fit the upper 200 m of measurements because these are affected by firn
67 compaction which introduces additional uncertainty.

68 The uncertainty in the difference in vertical position of the ApRES antennas is larger than the changes in
69 vertical position of the reflectors, such that a choice about the vertical velocity at the basal interface must
70 be made. If the bed is frozen, then the basal vertical velocity can be assumed to be zero such that the ApRES
71 measurements can be uniformly shifted (38). However, Dome C is potentially melting at the bed (39), so
72 the basal velocity may not necessarily be zero. The deepest 15 m of ApRES measurements show near zero
73 values, but from 15 to 30 m above the bed, the average is -0.0035 m a^{-1} , with an average of all 30 m of
74 -0.0022 m a^{-1} . Therefore, there are a number of different ways to fit the vertical velocity, by either shifting
75 the ApRES measurements, assuming a basal melt rate in the Lliboutry model fit, or both. Note that because
76 of the way a basal melt rate affects the vertical velocity profile, shifting the ApRES measurements by a
77 given value does not yield the same fit as imposing the same value as the modeled basal melt rate. We use
78 5 combinations of assumptions to find the range of potential of p values which are described in table S1.
79 This give a range of values from $p = 1.2$ to 3.2 with the surface vertical velocities ranging from 0.03 to
80 0.033 m a^{-1} . The range of p values is similar to the range found from inverse modeling of the depth-age
81 relationship (39). We use a value of $p = 2$ as our base scenario and $p = 1$ and 3.5 to define the range of
82 uncertainty. The surface velocities found in the fits are a few mm a^{-1} greater than the modern accumulation
83 rate. This could indicate a small component of vertical thinning (a meter to a few meters per 1000 years) or
84 the uncertainty associated with the ApRES measurements.

85 No ApRES data are available for the Dome Fuji site.

86 **S1.1.4 Ice-flow model forcing: accumulation rate**

87 The accumulation rate history is found using the best-fit vertical velocity profile to compute the thinning
88 function and the timescale for EDC. We use a hybrid timescale where the most recent 57 ka use the
89 timescale synchronized to WAIS Divide (40); prior ages are from AICC2012 (41, 42).

90 For Dome Fuji we use a similar approach in which the accumulation history is found using the thinning
91 function in combination with the timescale of ref. (43).

92 **S1.1.5 Ice-flow model forcing: surface temperature**

93 The surface temperature history is found from the modern temperature by scaling the temperature change
94 to the deuterium record (3, 43). The δD record is first interpolated to even spacing and smoothed with a
95 1000-year 7th order low pass filter. The surface temperature history, T_s , is found by

$$96 \quad T_s = T_0 + \Delta T_s \quad (\text{S4})$$

97 Where T_0 is the modern temperature and the change in surface temperature, ΔT_s , is found using equation
98 S5 following ref. (14):

$$99 \quad \Delta T_s(\delta) = \alpha_T^{-1} \int_t \delta(t) dt \quad (\text{S5})$$

100

101 where $\dot{\delta}$ is the time derivative of the filtered temporal δD record, t is time, and α_T the isotope sensitivity
102 (temporal slope). In all model results presented here, α_T is a constant and is not allowed to vary through
103 time.
104

105 **S1.1.6 Inverse procedure**

106 We use a gradient descent inverse method by defining the mismatch index:

$$107 \quad J = \int_0^H \frac{[T(z) - \Theta(z)]^2}{\sigma_{\Theta(z)}^2} dz \quad (S6)$$

108 where $T(z)$ are the modeled borehole temperatures, $\Theta(z)$ are the measured borehole temperatures, and $\sigma_{\Theta(z)}$
109 are the uncertainties in the measured borehole temperatures. The temperatures in the firn are excluded
110 (S1.1.2). The inverse procedure finds the values of T_{surface} , T_{bed} , and α_T , which all have a single optimum
111 value (i.e. unimodal distribution).

112 **S1.2 Results of temperature optimizations and uncertainty at Dome C**

113 We first discuss the borehole temperature reconstruction at Dome C, where we have the better data
114 constraints; we apply the lessons from Dome C to the Dome F reconstruction in Section S1.3.

115 We performed a series of optimizations for different prescribed ice properties and ice-flow parameters to
116 evaluate the most likely temperature change and its uncertainty. As described below, we consider two types
117 of uncertainty: (1) the temperature dependence of thermal conductivity (Section S1.2.1); and (2) parameter
118 and forcing history (Section S1.2.2). Our best estimate of the LGM (18-21.4 ka BP) minus PI (0.5-2.5 ka
119 BP) temperature change is $\Delta T_s = -5.5^\circ\text{C}$ based on the average of three relationships for the thermal
120 conductivity and our preferred forcings:

- 121 • a vertical velocity profile with $p=2$, based on ApRES vertical velocities (Section S1.1.3)
- 122 • 0.0005 m a^{-1} basal melting based on ref. (39)
- 123 • 100 m of deglacial thickening between 17 and 7 ka (Section S3.3)

124 The total uncertainty range is approximately $\pm 1.9^\circ\text{C}$, which is the sum of the thermal conductivity
125 uncertainty (Section 1.2.1, Table S2) and parameter/history uncertainty (Section S1.2.2, S1.2.3, Table S3
126 and Table S4).

127 **S1.2.1 Thermal conductivity**

128 The temperature dependence of the thermal conductivity (k) of ice is an important term for the inference of
129 the LGM-Holocene temperature change at low accumulation sites. The standard relationship in Cuffey and
130 Paterson (2010, p. 400) is from the review of Yen (1981), ref. (34). To evaluate the uncertainty due to the
131 thermal conductivity, we use the relationship from two data sets that were not used in the Yen (1981)
132 compilation (44, 45): Ross et al. (1978) and Waite et al., (2006). The thermal conductivity relationships are
133 plotted in Figure S2, with the full temperature range in the left panel and only the temperature range of
134 Dome C ice experiences in the right panel. Ross et al. (1978) reported only the fit, so the underlying data
135 cannot be plotted.

136 The inferred temperature change and misfit are given in Table S2 and shown in Figure S3. The choice of
137 relationship results in a 1°C difference in the inferred temperature change. Much of the model-data
138 temperature misfit occurs in the bottom 500m. The near-bed temperature gradient, where the temperature
139 gradient is nearly constant with depth, is not easily modeled. We test the impact of better fitting the near-
140 bed temperature by decreasing the temperature dependence of the thermal conductivity. We also performed

141 tests in which we add strain heat in the basal ice to better match the basal temperature; because these last
142 tests have the same impact as the changes in thermal conductivity on the inferred ΔT_s , we do not discuss
143 these model runs further.

144 To assess the influence of the thermal conductivity of the deepest ice, we perform tests in which we adjust
145 k for all ice with a temperature above -13°C . This temperature was chosen because it corresponds to the
146 depth at which the ice grain size and fabric shows a distinct change (46), which is thought to be associated
147 with the onset of migration recrystallization. The model-data fit is improved (Table S2) when we increase
148 k linearly by up to 5% for the basal ice (-2.18°C). It is not clear how the changes in grain properties might
149 impact k . Yen (1981) notes that k may be 5% greater along the c-axis of single crystals, which would be in
150 the opposite direction to what we have applied because the c-axis fabric is becoming less vertically oriented
151 near the bed (46); however, a study from the food science community suggests that the larger grain sizes
152 (associated with slower freezing rates in that study) can cause a decrease k of 10%, although they do not
153 report the grain sizes (47). While it is not clear how the change in grain properties should affect k , our
154 adjustment provides a useful way to assess its impact on the inferred ΔT_s . The closer match to the basal
155 temperature gradient allows the temperature misfit to be reduced. For each of the three published thermal
156 conductivity relationships, applying the 5% k adjustment changes ΔT_s by around 0.25°C .

157 The temperature measurement uncertainty is 0.01°C at EDC. Therefore, we consider RMS values within
158 0.02°C of each other as equally viable solutions, and thus cannot reject any of the thermal conductivity
159 relationships. We take the average of the six scenarios to define our best estimate of the magnitude of the
160 LGM-Holocene temperature change. We conservatively use the full range of the six scenarios (1.2°C) as
161 our uncertainty estimate.

162 **S1.2.2 Uncertainty from parameter choices**

163 We performed additional optimizations to assess the influence of the vertical velocity profile; the results
164 are given in Table S4 and Figure S4. The range of possible p values for the vertical velocity profile from
165 the ApRES measurements (S1.1.3) is very similar to published estimates (39). We use $p = 1$ and 3.5 as the
166 lower and upper bounds and a preferred p value of 2 . A smaller p value, which produces a vertical velocity
167 profile more like that beneath a stable divide where a Raymond Arch develops (48), yields a larger LGM-
168 Holocene temperature change, while a larger p value (more flank-like flow) yields a smaller temperature
169 change. The change in ΔT_s upon varying p values within the specified range is around 0.68°C (Table S4).
170 Note that surface accumulation rates are coupled to the vertical velocity profile via the thinning function.
171 When we alter the velocity profile, we alter the surface accumulation rates along with it to ensure internal
172 consistency. Therefore, the uncertainty in past accumulation rates is also included in our error estimates
173 (see Fig. S9 for the range of LGM accumulation rates in the borehole study).

174 The impact of basal melting was evaluated by assuming no basal melt or 1 mm/yr of basal melt instead of
175 0.5 mm a^{-1} based on Parrenin et al. (2007). No basal melt increases the magnitude of the LGM-Holocene
176 temperature change compared to the base scenario, while increasing the basal melt does the reverse. The
177 change in ΔT_s upon varying melt rates within the specified range is around 0.37°C (Table S4).

178 We base our choice of thickness change on published simulated thickness histories (49, 50). The impact of
179 deglacial ice sheet thickness changes was tested with alternative scenarios of either no thickness change, or
180 doubling the amount of thickening between 17 and 7 ka to 200m , roughly spanning the range of responses
181 seen in ice sheet model simulations (Section S3.3). Imposing no thickness change yields a 0.1°C larger ΔT_s .
182 Given the low sensitivity to the prescribed elevation, we did not evaluate specific inferences from individual
183 ice sheet models.

184 **S1.2.3 Temporal Variations in the shape of the vertical velocity**

185 The shape of the vertical velocity profile is not necessarily fixed in time. A potential influence on the shape
186 of the vertical velocity profile are changes in the temperature profile in the ice sheet; however, the low
187 accumulation rates lead to heat transfer being dominated by conduction and thus only minor temperature
188 variations deep in the ice sheet. Another potential influence is the development of a preferred crystal
189 orientation fabric; however, the ice fabric at interior East Antarctic sites evolves slowly because of the low
190 deformation rates (46) such that the evolution of the ice fabric is unlikely affect the vertical velocity pattern
191 during the glacial termination.

192 Instead, the most likely reason for the shape of the vertical velocity profile to change is the position of the
193 ice divide. As shown by the ApRES measurements and noted elsewhere (39), the shape of the vertical
194 velocity profile has more of a quadratic character, consistent with the influence of lower deviatoric stresses
195 near an ice divide (48), than the more linear shape predicted by Lliboutry (Eq. S2). This difference in shape
196 of the vertical velocity profile beneath divides is what gives rise to so-called Raymond Arches commonly
197 observed within coastal ice rises (51). No Raymond Arch is observed at EDC, likely due to the long
198 characteristic time (100 ka) for which the divide position would need to be stable. The core and the ApRES
199 measurements are near the ice divide today, such that any movement of the divide in the past would result
200 in the more linear (larger p value) shape typical for sites away from a divide.

201 We evaluate the impact of a temporal variation in the vertical velocity shape function with a range of
202 scenarios where we vary the onset time of the current vertical velocity profile ($p = 2$ for these scenarios)
203 and the shape of the previous vertical velocity profile. We allow the transition in vertical velocity shapes to
204 occur in 1 ka, at three different ages in the Holocene: beginning at 10 ka, 6 ka, and 2 ka. The previous shape
205 of the vertical velocity profile is not known, other than it should be more linear (more typical of a flank
206 site). We use $p = 4$, based on the vertical velocity profiles outside of the region of divide influence at
207 Roosevelt Island (38); $p = 7$ based on recent measurements from Hercules Dome, another interior Antarctic
208 dome site; and $p = 15$ which approximates a shape profile with deformation concentrated in the warm ice
209 near the bed. The inferred ΔT_S for the nine scenarios is shown in Table S3; these scenarios use the Yen
210 (1981) thermal conductivities and the standard forcing choices (S1.2); using the Waite et al., (2006) or Ross
211 et al., (1978) thermal conductivities gives the same change in the inferred ΔT_S to within hundredths of a
212 degree (34, 44, 45).

213 The inferred reduction in ΔT_S magnitude ranges from 0.44°C to 2.02°C with a mean reduction of 1.07°C.
214 Because the shape of the vertical velocity profile is always more linear (or flank-like) in the past, the
215 inferred ΔT_S is always smaller in magnitude. As the change in ΔT_S increases, the misfit to the borehole also
216 increases. Thus, it is not clear that a variable vertical velocity shape function yields a more robust solution.
217 Because we have no constraints on the shape of the vertical velocity profile for older ages and the timing
218 of a transition, it is difficult to produce a quantitative estimate of the potential impact. Therefore, we do not
219 directly include a temporally variable vertical velocity profile scenario in our “best estimate” independent
220 borehole ΔT_S estimate and uncertainty. However, the sensitivity test described in this section suggests an
221 asymmetrical source of uncertainty in the EDC borehole reconstruction, which we represent via an
222 estimated uncertainty range that is not centered around our best estimate of $\Delta T_S = -5.5^\circ\text{C}$ (but rather around
223 $\Delta T_S = -5.0^\circ\text{C}$, which is halfway between our best estimate and the mean of the tests described in this section).
224 We do note that the influence of time-variable p can reconcile the borehole- and Δage -based ΔT_S
225 reconstructions.

226 **S1.2.4 Additional temperature variability in borehole reconstructions**

227 As part of the borehole reconstruction, we performed a variety of optimizations with α_T allowed to vary for
228 different time periods. For example, in optimizations with two α_T scalings (one for the Holocene and one
229 for the remainder of the record which is dominated by the LGM-Holocene change), the Holocene scaling

230 was often very large (resulting in little temperature variability) while the glacial scaling remained similar
231 to that found in the single-scaling scenarios. Since the Holocene temperature variations are likely small,
232 they have diffused away in the borehole temperature profile and cannot be resolved. In addition, the near-
233 surface temperatures were less reliable such that the upper 150m were not included in the optimization,
234 which may also inhibit the ability to infer an independent Holocene scaling. This lack of high frequency
235 temperature information is a primary challenge of using borehole temperatures from low accumulation sites
236 compared to sites such as WAIS Divide (15). Only the broadest information of glacial temperature is
237 preserved, and we cannot reconstruct high frequency variations in the temperature history (25, 52).

238 **S1.3 Results of temperature optimizations and uncertainty at Dome Fuji**

239 We have performed a similar analysis for Dome Fuji as for Dome C; however, there are no ApRES vertical
240 velocity measurements at Dome Fuji, and temperature measurements have a five times higher uncertainty
241 at 0.05K. In addition, the ages and ice flow near the bed are not easily modeled, adding uncertainty in the
242 vertical strain pattern. In particular, Dome F has a reversal of the thinning function near the bed, which
243 layers in the deepest few 100 m having experienced less cumulative thinning than layers above it. In
244 addition, the DF core has inclined (up to 50°) internal layers in the deepest few 100 m, implying
245 inhomogeneous bottom melting in the vicinity (53).

246 Therefore, the confidence in the inference of LGM-Holocene temperature change is lower than at Dome C.
247 Our primary goal with the Dome Fuji borehole temperature measurements is to determine if they are
248 consistent with the smaller ΔT_S inferred with our firn-based reconstruction method.

249 We report two model runs that envelope a plausible range of the LGM-Holocene temperature change at
250 Dome Fuji based on the information from Dome C and previous modeling of Dome Fuji (39). Many more
251 runs were performed, but their ΔT_S falls within this envelope. Using parameters for a small ΔT_S – Yen
252 (1981) conductivity and no increase in basal thermal conductivity, a vertical velocity with $p=4$ and 0.3 mm
253 a^{-1} of basal melt – we obtain $\Delta T_S = -1.8^\circ C$. Using parameters for a large ΔT_S – Waite et al. (2006) thermal
254 conductivity with a basal increase up to 5%, $p=1$, and no basal melt – we obtain $\Delta T_S = -5.4^\circ C$. We thus
255 report this range of $-1.8^\circ C$ to $-5.4^\circ C$ as the ΔT_S that is consistent with the DF borehole data, without making
256 an attempt to provide a central or best estimate within this range as we feel that the problem is insufficiently
257 constrained to do so. The reader may be tempted to view the midpoint of the interval ($\Delta T_S = -3.6^\circ C$) as a
258 best estimate of DF cooling, but we do not endorse this interpretation.

259 The inferred DF ΔT_S range overlaps well with the firn-based reconstruction (Figure 1). The borehole
260 reconstruction suggests that ΔT_S at DF was likely smaller than ΔT_S at EDC, as also seen in the firn-based
261 reconstruction and climate model simulations. Importantly, the DF borehole reconstruction is inconsistent
262 with a large ΔT_S of around -7.5 to $-8^\circ C$, as suggested by traditional interpretation of the DF water isotope
263 data (8, 43).

264

265 **S2 Firn-based temperature reconstructions**

266 **S2.1 Ice Core data**

267 **S2.1.1 $\delta^{15}N$ - N_2 data**

268 Ice core $\delta^{15}N$ - N_2 data used in this study are all available from published work (30, 54-56), with the
269 exception of new Dome Fuji data first published with this paper (supplementary data). We combine ice
270 sample data and lock-in zone firn air data (where available). Site $\delta^{15}N$ - N_2 data are shown in Fig. 3C of the
271 main text. All $\delta^{15}N$ data use the modern atmosphere as the reference scale.

272 Unpublished Dome Fuji $\delta^{15}\text{N}$ data are generated in three measurement campaigns. The first campaign (at
273 Tohoku University, before 2001 (57)) covers 38 points from 563.3 to 992.9 m (LGM and older) with an
274 uncertainty of 0.02 per mil (1 sigma). The second campaign (at Scripps Institution of Oceanography, 2007,
275 (58)) covers 3 points from 462.5 to 478.5 m (Antarctic Cold Reversal) with uncertainty of 0.005 per mil.
276 The third campaign (at the National Institute of Polar Research, 2016 - 2018) covers 293 points from 113.0
277 to 558.0 m (Holocene and Termination I) with uncertainty of 0.006 per mil (manuscript for method in
278 preparation). There are offsets between the different datasets, thus 0.020 per mil is added to the Tohoku
279 dataset and 0.010 per mil is added to the SIO dataset to match them with the NIPR dataset where they are
280 overlapped.

281 For the SDM site we furthermore use published $\delta^{40}\text{Ar}$ data to calculate $\delta^{15}\text{N}$ -excess to constrain abrupt
282 warming at the 22ka event (59). An anomalous short-duration interval around 15.3 ka BP where SDM $\delta^{15}\text{N}$
283 approaches zero, thought to reflect a short-lived ablation event or catastrophic firn-break up (59), is
284 removed from the SDM $\delta^{15}\text{N}$ data set and not interpreted here.

285 **S2.1.2 CH₄ data**

286 Ice core atmospheric CH₄ mixing ratio data are used for ice core synchronization in the gas phase (Fig.
287 S5). Site CH₄ data were previously published for all sites except DF (16, 42, 60-62).

288 Dome Fuji CH₄ concentrations are measured at Tohoku University and Laboratoire de Glaciologie et
289 Géophysique de l'Environnement (LGGE, currently L'Institut des Géosciences de l'Environnement). The
290 Tohoku University data are collected in the same campaign as the $\delta^{15}\text{N}$ data using the method of ref (57)
291 with analytical uncertainty of ~6 ppb (1 standard deviation). For the LGGE data, the air is extracted from
292 the ice samples of ~50 g using an established melt-refreeze method, and analyzed by a gas chromatograph
293 using a standard gas (499 ppb) for calibration, and an analytical uncertainty of 10 ppb (1 standard deviation)
294 (60, 63). Before the synchronization, the LGGE dataset is shifted by +18 ppb to account for systematic
295 offset in calibration scale relative to the Tohoku University scale; note that we use CH₄ only to constrain
296 the event timing, and therefore the absolute concentrations are not important.

297 The SDM data used here are a compilation of previously published data (62, 64-68) measured at Oregon
298 State University and Seoul National University using the same methods described in refs. (64-67).

299 The full DF and SDM CH₄ records are provided in the data supplement.

300 **S2.1.3 Water isotope data**

301 Water isotopic $\delta^{18}\text{O}$ (rather than δD) data are used at all sites, reported on the Vienna standard mean ocean
302 water (V-SMOW) reference scale. These data are publicly available (3, 43, 64, 69-75). The ice core $\delta^{18}\text{O}$
303 data are corrected for the mean ocean $\delta^{18}\text{O}$ using ref. (76). The high-frequency structure in the firn-based
304 reconstructions (Fig. S8) comes from the $\delta^{18}\text{O}$ data, while our firn-based reconstruction method only
305 constrains magnitude of the long-term temperature change.

306 **S2.1.4 Siple Dome volcanic ties**

307 Volcanic tie points between the Siple Dome and WAIS Divide ice cores are given in the supplementary
308 data files. We identify a total of 18 such volcanic ties based on established techniques: nine ties are found
309 via matching Electrical Conductivity Measurement (ECM) records of volcanic activity (55, 77), and nine
310 ties via the geochemical identification of tephras (78, 79). The volcanic tie points are shown on Fig S5. The
311 oldest of these volcanic tie points is from 32ka BP, and thus the LGM and deglaciation are covered. Beyond
312 32ka we identify several ice-ice ties based on $\delta^{18}\text{O}_{\text{ice}}$ to extend the WD2014 chronology further back – these
313 tie points have no impact on the ΔT_s presented here.

314 **S2.2 Empirical Δ age reconstruction**

315 For all sites other than WD, we estimate Δ age empirically by combing ice-phase volcanic matching and

316 gas-phase atmospheric methane (CH_4) matching to WD (16). Site Δ age estimates are shown in Fig. 3B of
317 the main text. WD was chosen for this purpose because of the high resolution CH_4 record (80), and small
318 Δ age at the site (30). The matching procedure is shown in Fig. S5, where we show volcanic ties (dots) and
319 the site CH_4 records plotted on top of the WD CH_4 record. Volcanic ties to WD are published for all sites
320 except SDM (40, 42, 81-83); SDM ties are provided in the data supplement and described below.

321 Conspicuous CH_4 features – such as Dansgaard-Oeschger (DO) oscillations and the onset of the deglacial
322 CH_4 rise – are matched between the cores, thereby assigning a WD2014 gas age to the core being matched;
323 the WD2014 ice age at that same depth is found from the volcanically synchronized time scales (40),
324 allowing the gas age-ice age difference to be calculated. The sources of Δ age uncertainty are: (1) uncertainty
325 in the WD2014 Δ age; (2) uncertainty in the WD CH_4 tie point determination; (3) uncertainty in the matched
326 core CH_4 tie point determination (for example due to the finite time resolution of the CH_4 record); (4)
327 uncertainty in age scale interpolation between volcanic tie points; these 4 terms are added in quadrature to
328 estimate the Δ age uncertainty. Note that WD has the smallest Δ age of all cores considered here. The stated
329 2σ WD Δ age uncertainty is 120 years during the LGM; which is a 23% relative uncertainty. However, at
330 EDC the maximum Δ age during the LGM is around 5000 years, in which case the same 120-year
331 uncertainty only represents a relative uncertainty of 2.4%.

332 Figure S6 compares our empirical Δ age estimates (dots with errorbars) to the Δ age in the AICC2012 ice
333 core chronology (grey curves) for the cores where this is available (TAL, EDML and EDC), as well as the
334 Δ age simulated in this study using a firn densification model (colored curves). We find good agreement.

335 The approach outlined above provides WD2014-consistent Δ age estimates for all cores except WD; to apply
336 our firn-based approach to WD we have to generate independent empirical Δ age estimates. To do so we
337 use published bipolar volcanic markers for Holocene and glacial period (42, 84). We match the WD CH_4
338 record to the NGRIP $\delta^{18}\text{O}$ at the midpoint of abrupt DO transitions, assuming a 25-year lag of atmospheric
339 CH_4 behind Greenland climate (30, 85, 86); this provides a GICC05 gas age for each matched event, which
340 is combined with a GICC05 ice age at the same depth (found from the bipolar volcanic synchronization) to
341 calculate empirical Δ age WD estimates. The uncertainty in these Δ age markers is calculated as above for
342 the other cores. The most prominent CH_4 feature around DO-2 is actually associated with Heinrich event 2
343 rather than with DO-2 (80). A comparison of the WD CH_4 record to GISP2 CH_4 identifies the location of
344 the DO-2 CH_4 feature that is concurrent with the DO-2 thermal $\delta^{15}\text{N-N}_2$ fractionation signal (Fig S7B); this
345 allows us to establish an empirical WD Δ age constraint around this time by matching the WD CH_4 feature
346 to Greenland records on the GICC05 time scale. Figure S7A compares the WD2014 and GICC05 Δ age
347 reconstructions for WD; during the glacial the WD2014 Δ age is around 70 years smaller on average (84).

348 The differences between the two Δ age estimates for WD can be transferred to all the cores in this study,
349 and thus we have two sets of empirical Δ age estimates for each core: one consistent with the WD2014
350 chronology, and one with the GICC05 chronology. The influence of the choice of base chronology on ΔT_s
351 is estimated in the Monte-Carlo procedure (see below). The CH_4 match points, and the empirical WD2014
352 and GICC05 Δ age estimates (with uncertainty) derived from it, are provided in the data supplement.

353 For the SDM site we furthermore derive a Δ age constraint from the abrupt 22ka warming anomaly, which
354 is seen in both the ice phase ($\delta^{18}\text{O}_{\text{ice}}$) and gas phase ($\delta^{15}\text{N-N}_2$ and $\delta^{40}\text{Ar}$).

355 In the remainder we will refer to the empirical Δ age constraints as “ Δ age data” for the sake of brevity.

356 S2.3 Firn densification modeling

357 The rate of firn densification is sensitive to the temperature and the overburden pressure – with the latter
358 determined by the time-integrated snow accumulation rate since the deposition of a layer. The time-variably
359 surface temperature $T_s(t)$ and accumulation rate $A(t)$ histories are the primary controls on firn densification

360 rates, and firn densification models can be used to simulate the evolution of the firn layer through time (17,
 361 20, 87-91). The $\delta^{15}\text{N}-\text{N}_2$ and Δage become fixed at the lock-in depth, providing observational constraints
 362 on past densification rates (15, 88, 92). Critically, the $\delta^{15}\text{N}$ - and Δage -isopleths run perpendicular to each
 363 other in T_S, A -space (Main text Fig. 3A), meaning that if $\delta^{15}\text{N}$ - and Δage are both independently known, a
 364 unique temperature and accumulation solutions exist (20); however such solutions are obviously subject to
 365 any biases present in the firn densification physics used.

366 To simulate past Antarctic firn evolution, we use a dynamical firn densification – heat transport model
 367 described elsewhere in the literature (17, 30, 93, 94). For the firn densification physics we use the
 368 overburden-pressure formulation of the Herron-Langway firn model; given by Equation 4c in Ref. (18).
 369 The model can be run in an inverse mode, where an automated routine is used to find the $T_S(t)$ and $A(t)$
 370 solutions that optimize the fit to the $\delta^{15}\text{N}$ and Δage data; this approach was previously applied to Greenland
 371 records (17).

372 The inverse model adjusts the $T_S(t)$ and $A(t)$ input to minimize the cost function:

$$373 \quad S = \sqrt{\frac{1}{N_\delta} \sum_i \frac{(d_i - m_i)^2}{u_i^2}} + \sqrt{\frac{1}{N_\Delta} \sum_i \frac{(D_i - M_i)^2}{U_i^2}} \quad (\text{S7})$$

374 where d_i (D_i) are the $\delta^{15}\text{N}$ (Δage) data, m_i (M_i) the interpolated modeled values at the same depth, u_i (U_i)
 375 the data uncertainty, and N_δ (N_Δ) the total number of data. The climate forcings used in the modeling
 376 procedure are described by:

$$377 \quad T_S(t) = T_{\text{init}}(t) + f_T(t) \quad (\text{S8})$$

$$378 \quad A(t) = A_{\text{init}}(t) \times [1 + f_A(t)] \quad (\text{S9})$$

379 where T_{init} and A_{init} are the initial temperature and accumulation estimates; f_T and f_A are functions to correct
 380 our initial estimate, which are being optimized in the inverse modeling procedure. T_{init} is based on linear
 381 scaling of the site $\delta^{18}\text{O}$ (corrected for mean-ocean $\delta^{18}\text{O}$), using the isotope sensitivity constant α_{init} listed in
 382 table S5. The α_{init} values are chosen to be intermediate between the spatial slope α_S , and the LGM-PI α_T
 383 values reconstructed here (main text, Fig. 1). The reconstructed ΔT_S is independent of the choice of α_{init} in
 384 the 0.4 to 2.8 ‰ K^{-1} range that we have tested; the values used were found iteratively in two steps after a
 385 first attempt using the spatial slope isotope sensitivity as α_{init} . The choice of α_{init} mainly dictates the
 386 magnitude of high-frequency (decadal to millennial) temperature variability in the final reconstruction.
 387 Where available, A_{init} is based on de-strained layer-counted annual layer thickness data; this is only the
 388 Holocene at SP, and the last 31ka at WD. Elsewhere, A_{init} is likewise based on linear scaling of the water
 389 isotope record. All six variables in Eqs. (S8) and (S9) are plotted in Fig. S8.

390 The functions f_T and f_A are each defined using a series of control points a_i (white dots in Fig. S8), such that
 391 $f(t_i) = a_i$. At times in between the control points, the value of f is found via linear interpolation between the
 392 two adjacent control points. Because modern-day climatic conditions at the sites are known, we furthermore
 393 let $f(t=0) = 0$. Because our interest is in reconstructing ΔT_S , we decided to keep f_T (and in many cases f_A)
 394 constant through the duration of the LGM. This is implemented by requiring two adjacent control points to
 395 have the same value ($a_{i+1} = a_i$). This is indicated by thick grey horizontal bar connecting the two control
 396 points in Fig. S8. The values for a_i that minimize the cost function Eq. (S8) are found in an automated
 397 gradient method (17).

398 The timing of the control points was chosen to coincide with climatic change points in the $\delta^{18}\text{O}_{\text{ice}}$ records;
 399 for the deglaciation these are the onset of Heinrich Stadial (17.8 ka), the onset and termination of the
 400 Antarctic Cold Reversal (14.7ka and 12.8 ka), and the Holocene onset (11.6 ka). In other cases large features
 401 in the $\delta^{15}\text{N}$ record were used to select control points. Note that the number and timing of the control points

402 is different for each of the cores, as they were adjusted based on the unique characteristics and data
403 availability at each of the cores. In general, cores with more data ($\delta^{15}\text{N}$ and Δage) have a greater number of
404 control points.

405 As a first example of why certain control points were selected, we examine EDC and TAL where no $\delta^{15}\text{N}$
406 data are available older than ~ 23 ka BP. This means the $T_s(t)$ and $A(t)$ solutions are no longer uniquely
407 constrained at those ages, and therefore we require f_T to have a constant value for all t older than 18ka BP
408 (grey horizontal bars in Fig S8a and S8e). The model fits the EDC and TAL Δage observations prior to the
409 LGM through making adjustments to f_A instead (keeping f_T constant).

410 As a second example, consider the SDM core, which has a large upward shift in $\delta^{18}\text{O}$ around 21.4 ka BP
411 possibly driven by ice dynamics (59). We use control points on either side of the shift in both f_T and f_A to
412 allow the model to adjust both the temperature and accumulation change across this transition. The
413 transition is characterized by a large drop in $\delta^{15}\text{N}$ (the single largest feature in all $\delta^{15}\text{N}$ considered here),
414 and both warming and a reduction in accumulation rate are needed to fit this feature (Fig. S8g).

415 As a third example, consider the SP core. Due to its flank-flow configuration the accumulation rate is much
416 more variable than it would be at a dome, as the deposition site moves across spatial gradients in surface
417 accumulation (55, 95). For this reason, SP requires more accumulation control points than the other cores
418 do in order to fit the SP $\delta^{15}\text{N}$ data (Fig. S8d).

419 For the purpose of estimating ΔT_s the control points used during the deglaciation are most important. For
420 all sites we conducted sensitivity studies in which the number of control points during the deglaciation is
421 varied, and the changes in reconstructed ΔT_s are well within the spread estimated from the Monte Carlo
422 uncertainty approach (Section S2.4). Therefore, we do not report on these experiments separately.

423 Besides the $T_s(t)$ and $A(t)$ histories, the densification model requires other site-specific, user-defined
424 parameters (Table S5). The convective zone (CZ) thickness is estimated from firm air sampling data at all
425 sites except TAL where such data is not available and we use a generic value of 5m. The surface snow
426 density ρ_0 is estimated from density data at the sites. Following established methods (96), the lock-in density
427 is estimated by $\rho_{\text{LI}} = \rho_{\text{CO}} - \rho_{\text{diff}}$, with the temperature-dependent close-off density ρ_{CO} given by the
428 Martinerie equation (97), and ρ_{diff} a site-dependent lock-in zone thickness. We estimate ρ_{diff} from firm
429 density and firm air sampling data, and fine-tune the value to best fit modern-day Δage and $\delta^{15}\text{N}$ at the site.
430 It is established that lock-in zone thickness is proportional to site accumulation (98), and indeed we find
431 low ρ_{diff} values at the low-accumulation EDC and DF sites (4 kg m^{-3} and 3 kg m^{-3} , respectively) and higher
432 values at the high-accumulation WD site (10 kg m^{-3}). The recommended value for Greenland Summit is 14
433 kg m^{-3} (96). Intermediate-accumulation site SP has a thick lock-in zone, and we find an optimal ρ_{diff} of 15
434 kg m^{-3} . The ice sheet thickness H is taken as reported in the literature, and the site geothermal heat flux
435 (GHF) is estimated by fitting the borehole temperature profile – note that the GHF estimation given in Table
436 S5 is not optimized in any way, and therefore we recommend against interpreting these numbers. The GHF
437 estimates in table S5 are lower bounds to the true GHF, because the effect of ice melting at the bed is not
438 taken into account.

439 It has been hypothesized that dust (or perhaps calcium or fluorine/chlorine) may soften the ice, enhancing
440 densification rates (99-102). The effect is not included here, see section S2.5 for a justification.

441 The optimal solutions presented in the main manuscript are derived using the dynamical description of the
442 Herron-Langway (HL) densification model (18). However, other physical equations of firm densification
443 are available, and we want to assess how the choice of model influences the result (Fig. S9). We compare
444 the range of our dynamical HL Monte Carlo simulation (histogram, see also section S2.3 below) to results
445 from running the Arnaud (88, 103), Barnola (20, 87) and Bréant (89) firm densification models in the inverse
446 mode; we focus on the WD, EDC and DF sites that have borehole thermometry estimates (dots with error

447 bars). For all models we use the exact same experimental design: the same present-day T_S and A ; the same
448 T_{init} and A_{init} ; the same Δage and $\delta^{15}\text{N}$ data; and the same T_S and A control points. We adjusted the ρ_{diff} model
449 parameter for each model to obtain a good fit to the present-day Δage and $\delta^{15}\text{N}$ data, with the values given
450 in Table S6. The model-specific ρ_{diff} adjustments are similar at all sites, suggesting they reflect model biases
451 that are stable across a range of climatic conditions.

452 At WD, all models surveyed find a ΔT_S at WD in the -9.8 to -10.6°C range, consistent with the borehole
453 reconstruction. At EDC the HL and Bréant models find a ΔT_S that agrees with the borehole within
454 uncertainty; the Arnaud and Barnola models reconstruct a somewhat small ΔT_S . At DF all models are in
455 agreement within the borehole uncertainty range; yet again the Barnola and Arnaud models find smaller
456 ΔT_S . We find at both cold sites that the HL and Bréant models reconstructs a larger ΔT_S than the Arnaud
457 and Barnola models do, which is consistent with the fact that the former models have a lower effective
458 activation energy than the latter models (Fig. S9, right panel), meaning that it requires a larger temperature
459 change to induce the same change in densification rates. The Bréant model has a temperature-dependent
460 effective activation energy (implemented as the sum of three Arrhenius terms) and is a modification of the
461 Arnaud model (89); note that the Bréant model provides a much better fit to the borehole estimates than the
462 Arnaud model does suggesting it is indeed an improvement over the Arnaud model.

463 Past accumulation is well constrained in our method – better in fact than the temperature is (compare the
464 T_S and A envelopes in Fig. S8). The reason is an elemental physical one. The ice-equivalent lock-in depth
465 (LIDIE), accumulation rate, and Δage are linked via the simple equation $A = \text{LIDIE} / \Delta\text{age}$. LIDIE is a
466 scaled version of the lock-in depth (LID), and the scaling (of around 0.7) is very stable across a wide range
467 of climatic conditions (104). Because in our method both Δage and the LID (from $\delta^{15}\text{N}$) are known, the
468 accumulation rate is constrained very strongly. This is clearly visible in Fig. S9, where the four densification
469 models find almost identical LGM accumulation rates. Uncertainty in $\delta^{15}\text{N}$, Δage , ρ_0 , ρ_{diff} and CZ does
470 impact the reconstructed A slightly, which is investigated in the Monte-Carlo study (S2.4). The $A = \text{LIDIE}$
471 / Δage relationship is so fundamental that is independent of the firm densification model used to first order
472 – the firm model choice only controls the scaling between LIDIE and LID, which have a ratio very close to
473 0.7 in all models and all climates (104).

474 This comparison suggests that the dynamical HL and Bréant models provide results in good agreement with
475 the borehole temperature reconstructions over a large temperature range, and should therefore be given
476 preference in simulating Antarctic firm dynamics at cold locations.

477 S2.4 Monte-Carlo uncertainty estimation

478 To estimate the uncertainty in our ΔT_S estimates we use a Monte-Carlo (MC) approach in which we
479 randomly disturb the $\delta^{15}\text{N}$ and Δage data, and draw the user-defined model parameters randomly from a
480 prescribed distribution (Table S5). For 1000 such iterations we perform the model inversion to estimate the
481 $T_S(t)$ and $A(t)$, allowing us to describe the uncertainty in ΔT_S . Because inversion of the full dynamical HL
482 model is computationally expensive, we instead use the steady-state version of the HL model for the MC
483 uncertainty estimation. The procedure is identical to the dynamical model described above and uses Eqs.
484 (S7) to (S9) to solve for $T_S(t)$ and $A(t)$. The steady-state model does not calculate the temperature profile,
485 and we use a constant firm temperature gradient to account for thermal $\delta^{15}\text{N}$ fractionation by the GHF.

486 In each of the 1000 MC iterations we randomly draw each of the $\delta^{15}\text{N}$ data points from a normal distribution
487 with a mean equal to the observation, and a standard deviation equal to the uncertainty in that observation.
488 The Δage data points are each perturbed in two steps. In a first step we draw a random number c from a
489 uniform distribution between 0 and 1; all the Δage data points D_i for that iteration are set to a weighted sum
490 of the WD2014 and GICC'05-based Δage constraints (Fig. S7): $D_i = c \times D_i^{\text{WD2014}} + (1 - c) \times D_i^{\text{GICC'05}}$.
491 In the second step, we add a random perturbation to each of the D_i that is drawn from a normal distribution

492 of zero mean and a standard deviation equal to the uncertainty (U_i). The ρ_0 and ρ_{diff} parameters are drawn
493 from a normal distribution with a mean and standard deviation listed in Table S5. It has been suggested that
494 the convective zone may be climate dependent, and possibly thicker during the LGM. The convective zone
495 thickness is therefore described as the sum of two parts: 1) a climate-independent part that is randomly
496 drawn from a normal distribution with a mean and standard deviation as listed in Table S5 (in case of a
497 negative value, we re-draw until a non-negative value is obtained); 2) a climate-dependent part that is equal
498 to a scaled version of the site $\delta^{18}\text{O}$ record (such that it equals zero in the PI and one in the LGM) multiplied
499 by a random number drawn from a uniform distribution between 0 and 5 (the LGM CZ is thicker or equal
500 to the PI CZ).

501 The bias of the steady-state approach is calculated by taking the difference between the $T_s(t)$ and $A(t)$
502 solutions found in the dynamical HL inversion and the steady-state HL inversion, where both use the
503 preferred parameter settings; all steady-state HL solutions in the MC study were corrected for this bias. In
504 Figure 1 of the main text we report the mean and 2σ standard deviation of the ΔT_s distribution found in the
505 MC study – this differs from the dynamical HL solutions by 0.08°C on average.

506 **S2.5 The glacial $\delta^{15}\text{N}$ data-model mismatch in previous studies**

507 For several of the East Antarctic sites (EDC, DF, SP, EDML; see Fig. 3 of the main text) the firn thickness
508 during the glacial period as indicated by $\delta^{15}\text{N}$ is thinner than it is at present. However, densification models,
509 when forced with a ΔT_s of around -9°C , simulate a thicker glacial firn column (increased $\delta^{15}\text{N}$) than at
510 present. This has led to the notion that there is a $\delta^{15}\text{N}$ data-model mismatch in the glacial period in East
511 Antarctica (56, 89, 105, 106). Note however, that this behavior is not observed for the West Antarctic WD
512 and SDM cores that have increased glacial $\delta^{15}\text{N}$, nor at the TAL site (based on the limited available $\delta^{15}\text{N}$
513 data). Moreover, densification models have been very successful at simulating Greenland firn evolution
514 during the glacial time (17, 20, 90, 91, 107). Barring anomalous situations (such as surface melt and shear
515 zones of ice streams), we are not aware of a single study in which firn models fail to simulate the basic
516 properties of firn of interest here (meter-scale density, lock-in depth, Δage) within a reasonable error
517 margin.

518 One hypothesis for the low glacial $\delta^{15}\text{N}$ is a thickened CZ during the LGM (105, 106). To explain the low
519 glacial $\delta^{15}\text{N}$ requires up to 40m of CZ thickness during the LGM at DF (108). Such deep convective mixing
520 has not been observed in present-day Antarctica; the deepest documented CZ occurs at the extreme
521 Antarctic Megadunes site, a zero-accumulation site where deep thermal cracks act as conduits for air mixing
522 down to ~ 23 m depth (108). Glacial records of chemistry, water isotopes, volcanic deposition and
523 atmospheric composition of the cores used in this study all provide evidence for continuous and hiatus-free
524 ice accumulation through the glacial period, precluding the kind of conditions that drive deep mixing at
525 Megadunes. Also, low-accumulation dome sites (like e.g. Dome C) today tend to have thin rather than thick
526 convective zones. Overall there is limited support or evidence for this hypothesis (105).

527 Another proposed solution to the glacial $\delta^{15}\text{N}$ mismatch is linked to the hypothetical influence of dust (or
528 perhaps calcium or fluorine/chlorine) in softening the firn, thereby enhancing densification rates (99-102).
529 In this hypothesis, the high dust loading of glacial ice enhances densification rates, thereby thinning the firn
530 column as reflected in low glacial $\delta^{15}\text{N}$. At the WD site, where past $T_s(t)$ and $A(t)$ are well-constrained by
531 borehole thermometry and annual-layer counting respectively, it was found that including the effect of dust
532 softening only acted to deteriorate the fit to observational data (30). Recently, a multi-site study found that
533 while including dust softening improved the model-data agreement at EDC and EDML, it worsened the
534 agreement at WD and the Greenland NGRIP site (89). Generally, in Greenland cores, where dust loading
535 is an order of magnitude larger than in Antarctica, densification models are successful in simulating firn
536 evolution without taking the hypothesized softening effect of dust into account (17, 20, 90, 91, 107). If the
537 hypothesized dust softening effect were true, it should work at all locations and time periods; since it does
538 not, we believe this hypothesis can be eliminated.

539 LGM climate in interior East Antarctica has no modern analogues, and therefore falls outside the calibration
540 range of densification models – perhaps casting doubt on their ability to simulate such climates (note that
541 this cannot be a complete solution to the “glacial $\delta^{15}\text{N}$ problem”, because EDML, SP and Law Dome all
542 exhibit low glacial $\delta^{15}\text{N}$, yet remain within the densification model calibration range). Bréant et al. provide
543 an interesting variation on this idea, by suggesting that firn densification models are too sensitive to
544 temperature at cold conditions (89). They re-tune the Arnaud model to reduce its sensitivity at low
545 temperatures, thereby improving the fit to glacial $\delta^{15}\text{N}$ data. There are two important caveats: (1) they
546 invoke a hypothetical densification process with an activation energy of 1.5 kJ/mol – at least 10 times
547 smaller than any known densification or vapor movement processes in firn; (2) the model (when forced
548 with $\Delta T_s = \sim -9^\circ\text{C}$) still requires dust softening to satisfactorily fit $\delta^{15}\text{N}$ data at EDML and EDC (89), as
549 well as at DF (Anaïs Orsi, personal communication 2019). In our analysis, the performance of the Bréant
550 model at low temperatures is very comparable to the HL model (Fig. S9).

551 Our work suggests an alternative solution to the glacial $\delta^{15}\text{N}$ data-model mismatch: all previous firn
552 modeling work has overestimated glacial cooling in East Antarctica. We find that the HL densification
553 model can fit Δage and $\delta^{15}\text{N}$ data for all Antarctic core sites using $T_s(t)$ forcing consistent with the borehole
554 temperature profiles, and $A(t)$ forcing consistent with de-strained layer thickness. The spatial ΔT_s pattern
555 we find correlates well ($r=0.90$) with that in GCM simulations using realistic Antarctic LGM topography.

556 Our work uses the HL densification model, which is calibrated over a temperature range from -15°C to
557 -57°C (18). The lowest LGM temperatures in our reconstructions are -60°C (Dome F), which is just outside
558 the HL calibration range. However, for the two coldest sites (EDC and DF) our firn-based ΔT_s is in good
559 agreement with the borehole temperature profile (main text Fig. 2), suggesting the model performs
560 adequately under such cold climatic conditions. Moreover, ΔT_s at the cold DF site is very similar to ΔT_s
561 at the nearby EDML site, where LGM temperatures of around -50°C are well within the HL calibration range.

562

563 **S3 Climate model simulations**

564 **S3.1 HadCM3 model**

565 We use the fully coupled ocean-atmosphere model HadCM3B M1 (109, 110). This model has a long history
566 of use in paleoclimate simulations, more recently, has been found very useful for sensitivity testing past
567 climates (111-114). Briefly, the atmosphere model has a horizontal resolution of 96×73 gridpoints
568 (3.75° longitude $\times 2.5^\circ$ latitude) with 19 hybrid levels (sigma levels near the surface, changing smoothly to
569 pressure levels near the top of the atmosphere). The ocean component has a horizontal resolution of
570 288×144 grid points ($1.25^\circ\times 1.25^\circ$) and in the vertical there are 20 depth levels.

571 The HadCM3 model simulations presented here are extended from a more than 5000 year long LGM
572 simulation of the model using the PMIP2 protocol (111, 115). This is broadly similar to the PMIP3 (116)
573 protocol (GHG, land sea mask, vegetation) but differs in the ice sheet reconstruction: PMIP2 uses ice5G,
574 PMIP3 uses a composite (116). In our simulations, since we vary the Antarctic topography, the difference
575 between the PMIP2 and PMIP3 lies only in the topography of the Northern Hemisphere ice sheets. HadCM3
576 has a climate sensitivity (global warming in response to doubling of CO_2) of around 3.5°C ; the LGM
577 simulation has an Atlantic Meridional Overturning Circulation (AMOC) strength of ~ 17.2 Sv.

578 All sensitivity simulations (section S3.3) are run for an additional 500 years (on top of the LGM spin-up)
579 with the analysis performed on years 50-150. There are negligible differences between results for any 100
580 year period after an initial 50 year spin up.

581 LGM surface atmosphere cooling in HadCM3 is -5.4°C in the global mean; -3.2°C in the tropics (30°S -
582 30°N); -10.6°C in the northern hemisphere extratropics, and -5.0°C in the southern hemisphere extratropics.

583 Northern hemisphere extratropical surface cooling is much greater than other zonal bands due to the large
584 albedo and lapse-rate forcing of the large NH ice sheets (Laurentide and Fennoscandian).

585 **S3.2 MIROC model**

586 We further perform numerical experiments with the Model for Interdisciplinary Research on Climate 4m
587 (MIROC4m) AOGCM (117). This model consists of an atmospheric general circulation model (AGCM)
588 and an oceanic general circulation model (OGCM). The AGCM solves the primitive equations on a sphere
589 using a spectral method. The horizontal resolution of the atmospheric model is $\sim 2.8^\circ$ and there are 20 layers
590 in the vertical. The OGCM solves the primitive equation on a sphere, where the Boussinesq and hydrostatic
591 approximations are adopted. The horizontal resolution is $\sim 1.4^\circ$ in longitude and 0.56° to 1.4° in latitude
592 (latitudinal resolution is finer near the equator). There are 43 layers in the vertical. Note that the coefficient
593 of horizontal diffusion of the isopycnal layer thickness in the OGCM is slightly increased to $700 \text{ m}^2\text{s}^{-1}$
594 compared with the original model version ($300 \text{ m}^2\text{s}^{-1}$) that was submitted to PMIP2. The current model
595 version has been used extensively for modern climate, paleoclimate (118), and future climate studies (119).
596 The climate sensitivity of this model is 4.3°C (119); the model has an LGM AMOC strength of $\sim 7 \text{ Sv}$, a
597 shoaled mode of northern source deep water in the Atlantic and expanded southern source deep water, in
598 good agreement with reconstructions based on North-Atlantic $\delta^{13}\text{C}$ and $\Delta^{14}\text{C}$ marine sediment data (120).

599 Ice sheet topography sensitivity experiments are initiated from a previous LGM experiment (53, 120),
600 which is forced with PMIP3 boundary conditions (116). Based on this original experiment, the topography
601 of the Antarctic ice sheet is modified following multiple reconstructions (Section S3.3); the extent of
602 Antarctic ice sheet is unchanged from the original PMIP3 LGM experiment. These sensitivity experiments
603 are integrated for 1000 years and the climatology of year 401-500 is used for analysis. The main result does
604 not depend on the choice of the period used for the analysis.

605 LGM cooling in MIROC and HadCM3 is respectively -5.2°C in the global mean; -2.7°C in the tropics
606 (30°S - 30°N); -12.7°C in the northern hemisphere extratropics, and -3.1°C in the southern hemisphere
607 extratropics. Northern hemisphere extratropical surface cooling is much greater than other zonal bands due
608 to the large albedo and lapse-rate forcing of the large NH ice sheets (Laurentide and Fennoscandian).

609 **S3.3 Ice sheet topography sensitivity experiments**

610 We perform a series of sensitivity experiments with both models in which we vary the shape of the LGM
611 ice sheet over Antarctica using a variety of reconstructions. For all of these LGM ice sheets we vary the
612 topography but not the ice sheet extent (or ice mask), to ensure that we are only investigating the
613 contribution of topography and not the albedo contribution to regional surface temperatures. For some
614 reconstructions this results in a less extensive ice sheet in Antarctica, for others a more extensive ice sheet.
615 In these latter cases the additional ice is set to 5m elevation. When adjusting the Antarctic ice sheet we
616 follow the PMIP protocol of adding the LGM to preindustrial elevation anomaly to the models preindustrial
617 topography. Since the PI topography in some reconstructions used is not the same as preindustrial
618 topography in the climate model, this means that the absolute LGM topography in these cases differs
619 between the climate model and the original reconstruction; the LGM-PI ice anomaly is the same as in the
620 original publications, however.

621 To isolate the climatic and topographic contributions to LGM cooling, we furthermore run an LGM
622 simulation in which we use full LGM boundary conditions (including LGM Antarctic ice mask), but PI
623 topography in Antarctica. In this simulation we keep the ice sheet elevation constant relative to the modern
624 geoid; since the LGM sea level was 120 m lower than during the PI, this means that in this simulation the
625 ice sheet elevation is 120 higher relative to the contemporaneous sea level.

626 We perform LGM climate model simulations with 8 different ice sheet topographies; 7 from LGM ice sheet
627 reconstructions (29, 50, 116, 121-125) and the last being the PI topography. All the LGM-PI ice elevation
628 anomalies are shown in Fig. S10, expressed relative to the PI geoid rather than contemporaneous sea level

629 (hence the 120 m elevation drop over the Southern Ocean). Each of these topographies was used to force
630 both the MIROC and HadCM3 climate models, with the simulated ΔT_s shown in the right two columns of
631 Fig. S10. Unless noted otherwise, we only consider the first five of the LGM topographies shown in Fig.
632 S10 in our analyses. The other two are only shown here for completeness and historical reasons; the Ice-
633 5G reconstruction has been superseded by Ice-6G, and the PMIP3 ice sheet has highly unrealistic ice
634 loading (up to 2500 m surface elevation gain) over interior West Antarctica.

635 For all topographies (main text Fig. 1, Fig. S10), the HadCM3 model on average simulates 2.2°C more
636 LGM cooling than MIROC does across Antarctica (except for SDM). The same difference is seen in the
637 SH extratropical (90°-30°S) zonal averages given earlier. The core site average ΔT_s is -6.3 ± 0.7 °C in
638 MIROC and -8.5 ± 1.1 °C in HadCM3 (2σ spread between topographies); it is -6.6 ± 1.8 °C in our firn-based
639 reconstructions (Fig. 1, main text). The MIROC model thus matches our reconstructions more closely on
640 average – the only exception is the WD site. The PMIP4 multi-model ensemble has a core site average ΔT_s
641 of -7.8 ± 4.6 °C using the Ice-6G topography.

642 Next we address the ΔT_s spatial pattern, which is due to a combination of a lapse rate effect due to the
643 elevated topography and a dynamical effect caused by changed atmospheric circulation again due to the
644 elevated topography. The overall effect of ice sheet topography is comparable between the models, with
645 both models showing a lapse-rate cooling with increased site elevation following a lapse rate of around -
646 10°C km^{-1} , close to the dry adiabatic lapse rate (main text, Fig. 4d).

647 Figure 1 of the main text compares the simulated ΔT_s from both models to the data-based reconstructions.
648 In terms of the absolute changes, MIROC provides a better fit to the reconstructions than HadCM3 does,
649 with the exception of the WD site where HadCM3 provides the closer fit. In terms of the spatial pattern
650 both models perform equally well; we find a Pearson correlation of $r = 0.86$ between the firn-based ΔT_s and
651 the HadCM3 simulation (average of 5 topographies), and for MIROC this is 0.88; when averaging both
652 models, the correlation increases to 0.96. Of all the topographies considered, Pollard and DeConto (2009)
653 and Whitehouse *et al.* (2013) give the best correlations (0.96 and 0.91, respectively). For the models in the
654 PMIP4 LGM ensemble (section S3.6), we find correlations ranging from $r = 0.46$ to $r = 0.93$ (average
655 single-model $r = 0.79$); interestingly, when averaging the models we again find an increase in correlation
656 to $r = 0.95$, which is higher than for any of the individual models. It is clear that AOGCMs broadly match
657 the spatial pattern seen in the firn-based reconstructions.

658 **S3.4 Isotope-enabled CESM model simulations**

659 The LGM and preindustrial simulations used the water isotope-enabled Community Earth System Model
660 version 1.3 (iCESM1.3) with a horizontal resolution of $1.9 \times 2.5^\circ$ (latitude \times longitude) for the atmosphere
661 and land, and a nominal 1° for the sea ice and ocean. The physical climate model of iCESM1.3 is an
662 upgraded version of CESM1 (126) with small changes in the atmosphere component. The water isotope
663 capability of iCESM has been documented and validated against present-day and paleoclimate observations
664 (127).

665 The iCESM1.3 LGM simulation was performed following the protocols from the Paleoclimate Modelling
666 Intercomparison Project phase 4 (PMIP4) with the LGM (at 21ka) values of greenhouse gas concentrations,
667 Earth orbital parameters, and the ICE-6G reconstruction of land ice sheets (19, 125). Ocean state in the
668 simulation was initialized from an existing equilibrated LGM simulation that used an older version of
669 CESM (128). The isotopic composition of seawater was initialized from the Goddard Institute for Space
670 Studies observations with a constant value of 1.05‰ added to account for the glacial enrichment due to the
671 increased LGM ice sheets. The iCESM1.3 LGM was integrated for an additional $\sim 1,000$ years. The TOA
672 energy imbalance averaged over the last 100 years is approximately -0.1 W m^{-2} , indicating the surface
673 climate has reached a quasi-equilibrium glacial state. Readers are referred to ref. (129) for details of the
674 LGM and corresponding preindustrial simulations.

675 **S3.5 Brief review of published isotope-enabled LGM simulations**

676 LGM to present water isotope changes in Antarctica depend on many key factors including (but not limited
677 to) southern hemisphere SST patterns (6), sea ice extent (7), ice sheet elevation (8), atmospheric transport
678 pathways (130, 131), precipitation seasonality (132), stratosphere-troposphere vapor exchange (133) and
679 post-depositional snow redistribution and snow-vapor isotope exchange (9, 134). Isotope-enabled general
680 circulation models (iGCMs) seek to capture the aforementioned physical processes making them an
681 invaluable tool in understanding isotopic variations in Antarctica. However, most if not all of the above-
682 mentioned factors have large uncertainties associated with them, and some processes are not typically
683 simulated in iGCMs (such as stratospheric exchange and post-depositional isotopic exchange). iGCMs
684 typically capture the present-day spatial slope well (2), yet $\delta^{18}\text{O}$ offsets at individual sites of 10 ‰ or more
685 (i.e. twice the LGM-PI $\delta^{18}\text{O}$ difference) are not uncommon.

686 Owing to both the complexity of the system and the large uncertainty in individual components, iGCMs
687 simulate a wide range of values for the temporal slope α_T (here: the ratio of the LGM-PI change in $\delta^{18}\text{O}$ of
688 precipitation over ΔT_S). Considering only studies that investigate the LGM-PI difference, iGCMs have
689 suggested α_T values in central East Antarctica that are:

- 690 - in the 0.1 to 0.6 ‰ K^{-1} range, and thus considerably lower than the spatial slope (6, 8, 11, 135)
- 691 - in the 0.6 to 0.9 ‰ K^{-1} range and thus comparable to the spatial slope (5, 6, 8, 12, 136)
- 692 - in the 0.9 to 1.6 ‰ K^{-1} range and thus considerably larger than the spatial slope (12, 137) (this study)

693 Note that it is not trivial to compile the temporal slopes consistently, given that papers report values at
694 different locations and time intervals, and the fact that the simulated temporal slopes tend to be highly
695 variable between nearby location (8, 138). A systematic iGCM intercomparison would be highly valuable
696 to the field. Studies that are listed more than once may report results from different models, models run
697 under different boundary conditions, or have large differences between central East Antarctic core sites.

698 It is very challenging to assess how the full uncertainty in all the aforementioned processes influences the
699 simulated α_T . However, the inter-model spread can serve as an uncertainty estimate of how well the various
700 processes are constrained in the models. We remove the high and low extremes from the simulated α_T
701 range, and estimate that central East Antarctic LGM-PI α_T as simulated by iGCMs is in the 0.3 to 1.4 ‰
702 K^{-1} range. For EDC and DF this implies a surface temperature ΔT_S of 4°C to 21°C, and 4°C to 18°C,
703 respectively (rounded to nearest integer, and ice core $\delta^{18}\text{O}$ corrected for mean ocean $\delta^{18}\text{O}$).

704 **S3.6 Paleoclimate Modeling Intercomparison Project Phase 4 (PMIP4)**

705 Here we use the multi-model LGM ensemble from the PMIP4 project, which includes the following 10
706 models: AWI-ESM1, AWI-ESM2, CCSM4-UofT, CESM1.2, iLOVECLIM1.1.1 (GLAC-1D),
707 iLOVECLIM1.1.1 (ICE-6G-C), INM-CM4-8, IPSL-CM5A2, MIROC-ES2L, and MPI-ESM1.2. All
708 models use the Ice-6G LGM ice sheet topography (125) except for iLOVECLIM1.1.1 (GLAC-1D), which
709 uses the GLAC-1D model (29). For a description of the PMIP4 LGM experiment, a description of the
710 various models, and an assessment of their performance, we refer to previous work (19, 139).

711

712 **S4 Elevation change from ice core Total Air Content data**

713 **S4.1 Data description and cut-bubble correction**

714 We use total air content (TAC) data as a paleo-elevation proxy from the WD, EDC and DF sites. Data from
715 EDC were previously published (22), for WD and DF we present previously unpublished data.

716 For the DF core we use two separate data sets. A first series of measurements were carried out at LGGE/IGE,
717 Grenoble, France, using an original barometrical method implemented with an experimental setup called

718 STAN (140). The STAN allows precise evaluation of the pressure and temperature of air extracted from an
719 ice sample by its melting-refreezing under a vacuum in a volume-calibrated cell. After correcting the
720 measured pressure for the partial pressure of saturated water vapor and of the calibrated volume for the
721 volume occupied by refrozen bubble free ice, the TAC is calculated using the ideal gas law. The ice samples
722 used in STAN have a mass of about 25 g and a regular shape of a rectangular parallelepiped or cube, which
723 facilitates estimation of their specific surface. A second, independent dataset of DF TAC was generated at
724 Tohoku University (TU), Sendai, Japan, as part of the gas chromatography measurements (57, 141). Briefly,
725 an ice sample of ~300 g was melted in a vessel under vacuum, and the extracted air was transferred to a
726 sample tube after removing water vapor. The pressure of the sample air was measured at room temperature
727 in a combined volume consisting of the sample tube, gas chromatograph inlet and sample loops, with a
728 semiconductor pressure transducer. The volumes of the sample tubes and other parts were calibrated prior
729 to the ice core measurements, and the temperature and pressure of the laboratory were used for normalizing
730 the results. The latter data set was scaled linearly by 0.975 to bring it into agreement with the calibrated
731 STAN data set; the origin for the discrepancy is not clear, but we note that the two datasets agree excellently
732 in terms of relative variations

733 Both DF datasets were corrected for the “cut-bubble effect”, which is the gas loss from air inclusions
734 (bubbles, gas hydrates and relaxation features such as air cavities) cut at the surface of the sample. The
735 correction depends on the specific surface of the ice sample and the size of air inclusions (142). The size of
736 air inclusions was measured under a binocular microscope in 2-4 mm thick sections of ice cut in parallel
737 with the samples used for STAN measurements; for the gas chromatography data set we used linear
738 interpolation to find the bubble diameter at the sample depths.

739 The absolute precision of the STAN TAC measurements has been estimated to be within $\pm 0.6\%$, and of the
740 gas chromatography TAC measurements better than 1%. However, the overall error of the obtained TAC
741 values amounts to 1% due to the uncertainties in the cut-bubble correction. The average reproducibility of
742 the STAN measurements performed in the same horizontal slice of an ice core has been confirmed to be
743 better than 1%.

744 WAIS Divide TAC and methane were measured concurrently at Oregon State University using a wet-
745 extraction process following ref. (143) with minor changes; the method is similar to those used elsewhere
746 (97, 144). The measurements presented were made over intervals between 2006 to 2017. The sample size
747 was 50 to 60 g, and the majority of samples were run in duplicate. The melt-refreeze process does not
748 extract all air, and a solubility correction is applied. The size of the correction is found by performing a
749 second melt-refreeze extraction on the frozen sample water, which allows estimating the magnitude of the
750 dissolved air fraction. The solubility correction as a percent of the initial pressure is determined to be $1.3 \pm$
751 0.2% for Holocene samples and $1.3 \pm 0.1\%$ for the deeper samples. Replicate analyses suggest a
752 reproducibility of better than 0.5%. As for DF, we correct for the cut-bubble effect following ref. (142). We
753 assume uniformly distributed spherical bubbles using published bubble radius data (145). Beyond 562m
754 depth, radius values are extrapolated using a linear fit with the bubble correction estimated to be 0 at 1600m
755 due to the completion of the bubble-clathrate transition.

756 Panel S12d compares TAC signal differences between the LGM and PI, where we have subtracted the PI
757 mean TAC value from the records (thereby aligning them during the PI). We find that during the LGM,
758 TAC at EDC and DF was elevated relative to the TAC at WD; the difference is around 7 mL kg^{-1} for DF-
759 WD, and 6 mL kg^{-1} for EDC-WD.

760 **S4.2 Data corrections and Elevation change**

761 It is challenging to interpret TAC in terms of absolute elevation change; our approach instead aims to
762 reconstruct the difference in LGM elevation anomaly Δz between WAIS and EAIS (which we term $\Delta\Delta z$).
763 Quantitative interpretation of TAC is possible because: (1) we investigate relative changes in TAC between

764 WD and DF/EDC, which means that the large influence of insolation on both records cancels out to first
765 order; and (2) we only investigate the LGM and PI time slices, both of which are equilibrium firm states not
766 impacted by transient TAC anomalies due to changes in overburden pressure and/or changing firm
767 temperature gradients (146).

768 To convert the TAC data into elevation change, we first need to apply several corrections. The first and
769 most critical is the correction for insolation (22). Because we are interpreting relative TAC changes (WD
770 vs. EDC/DF) rather than absolute ones, most of the insolation signal is canceled out because it affects TAC
771 records at both locations. However, the elevation component of TAC is recorded on the gas age scale, while
772 the insolation component of TAC is recorded on the ice age scale, and hence the cancellation effect is
773 incomplete. To account for this, we apply an insolation correction based on the integrated summer
774 insolation (Fig. S12c) as is the standard in the literature (22, 146). Eicher et al. (2016) report a sensitivity
775 of $-5.7 \text{ mL kg}^{-1} \text{ GJ}^{-1}$ at NGRIP (146), while the data from Raynaud suggest a sensitivity of -6.6 mL kg^{-1}
776 GJ^{-1} at EDC. Here, we shall use the average of these two estimates as our optimal correction scenario. To
777 assess the uncertainty in the correction, we furthermore construct a scenario with no insolation correction,
778 and a scenario in which we use a correction that is twice as large as the optimal scenario.

779 A second correction is for the temperature at bubble close-off, which impacts TAC in two ways: (1) it
780 changes the pore volume at close-off, which we calculate using ref (97); and (2) it impacts the number of
781 moles trapped at a given volume and pressure via the ideal gas law. These two effects cancel each other out
782 almost completely; the LGM TAC correction is 0.001, 0.0005, and 0.0004 mL kg^{-1} at WD, EDC and DF,
783 respectively.

784 Third, TAC reflects the elevation of the close-off depth, and not the ice surface of interest. We apply a
785 correction using the simulated close-off depth from the firm model, which is well-constrained by $\delta^{15}\text{N}$ data.
786 The LGM close-off depth anomaly relative to the PI was +7 m, -12 m, and -8 m at WD, EDC and DF,
787 respectively. We do not assess the uncertainty in the close-off depth correction given that it is negligible
788 compared to the uncertainty in the insolation correction.

789 The TAC changes are then converted to relative elevation change ($\Delta\Delta z$) using the pressure-elevation
790 relationship over Antarctica (147), and listed in Table S7 – note that the three insolation correction scenarios
791 are listed separately. For each insolation scenario, and for each combination of cores (either WD-EDC or
792 WD-DF) we calculate a lower bound $\Delta\Delta z$ by assuming the entire WAIS-EAIS air content change is solely
793 due to elevation change at WD (with EDC/DF elevation stable), and an upper bound $\Delta\Delta z$ by assuming the
794 entire WAIS-EAIS air content change is solely due to elevation change at EDC/DF (with WD elevation
795 stable) – the reason these two provide an lower and upper bound respectively is because a given TAC
796 change represents a larger fractional change at the higher elevation EDC/DF sites than it does at WD. We
797 also list a “weighted mean”, in which we convert the LGM-PI change in WD TAC as if it reflects elevation
798 change at WD, and the LGM-PI change in EDC/DF TAC as if it reflects elevation change at EDC/DF.

799 We here report a best-estimate $\Delta\Delta z$ of 420 m, with a conservative range of 280 – 590 m; these values are
800 labeled with the letters C, L and U in Table S7, respectively, and given with two significant digits. In order
801 to visually compare our TAC-based estimates to the model-simulated LGM topography anomaly (Fig. 4c),
802 we added a constant elevation change to our TAC-based estimates such that it minimizes the root-mean-
803 square (RMS) offset between the ice sheet model-simulated (Section S3.3) and TAC-based topography
804 anomaly; this yields an LGM elevation anomaly of +310 m, -80 m, and -140 m at WD, EDC and DF,
805 respectively (2 significant digits).

806 By calculating the RMS offset, we find that the ice sheet simulation by Whitehouse et al. (2012) provides
807 the closest agreement (RMS offset of 13 m) to our TAC-based $\Delta\Delta z$, with a $\Delta\Delta z$ of 403 and 457 m for WD-

808 EDC and WD-DF, respectively (compare to 388 and 445 m, table S7). The next-best model is ICE-6G,
809 which has an RMS offset of 60 m.

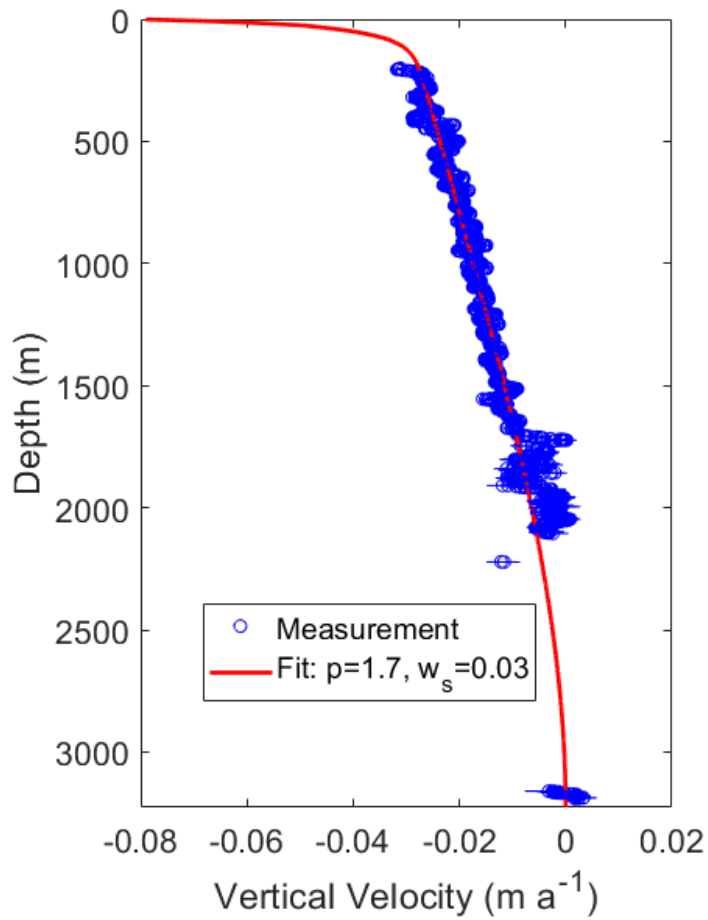
810 **S5 Occam's Razor**

811 Below we list reasons why we believe our reconstructions should be preferred in future interpretation of
812 Antarctic LGM surface climate, rather than the traditional water isotope scaling method in which the
813 modern spatial slope is used.

- 814 (1) Complexity: water isotopes are part of a complex system that involves the hemispheric-scale
815 hydrological cycle including sea ice, SST, atmospheric transport, ice topography, etc; several of these
816 changes are poorly constrained. By contrast, firn densification and ice flow are more simple physical
817 systems with only local influences, that can be studied in detail today over a wide range of climatic
818 conditions.
- 819 (2) Boundary layer inversion: Small fractional changes to the LGM inversion strength (as simulated in
820 most climate models) complicate the reconstruction of ΔT_S from water isotopes. Both our methods
821 unequivocally reconstruct firn temperature, making the results easier to interpret. A small ΔT_S in central
822 East Antarctica is broadly consistent with water isotope observations via GCM-simulated changes to
823 the LGM inversion (Fig. 4f, Fig. S11).
- 824 (3) Consistency: isotope-enabled models simulate LGM-PI temporal slopes that range roughly from 0.3 to
825 1.4 ‰K^{-1} in central East Antarctica (Section S3.5) which would imply a ΔT_S in the range of 4 to 20°C .
826 By contrast, when comparing four different densification models in our Δage -based method, we find a
827 range (largest minus smallest) of reconstructed ΔT_S of 0.78°C at WD, 1.70°C at EDC, and 1.18°C at
828 DF. The stated 95% confidence range (upper minus lower bound) is 3.8°C at WD, 3.8°C at EDC, and
829 3.4°C at DF for the borehole method; and 2.6°C at WD, 3.0°C at EDC, and 4.0°C at DF for the Δage
830 method. The borehole- and Δage -based reconstruction methods agree within uncertainty at all sites. It
831 is clear that our reconstruction methods show more consistency and agreement than isotope-enabled
832 GCMs do.
- 833 (4) Elevation change: Air content data and ice sheet reconstructions all suggest that the LGM elevation
834 anomaly in West Antarctica is several hundred meter higher than that in central East Antarctica (air
835 content suggests 280 to 590 m); this implies a difference in ΔT_S via the lapse rate. The PMIP4 model
836 ensemble mean finds that ΔT_S at WD minus the ΔT_S in central East Antarctica (here mean of DF and
837 EDC) is around $-5.9 \pm 2.7^\circ\text{C}$, in good agreement with our reconstructions ($-6.1^\circ\text{C} \pm 2^\circ\text{C}$); using
838 traditional water isotope scaling this difference is only -2 to -3°C , which is harder to reconcile with the
839 elevation changes.
- 840 (5) Firn data: The traditional interpretation of isotope data ($\Delta T_S \approx -9^\circ\text{C}$) leads to inconsistencies in
841 simulated firn thickness ($I05$), despite the fact that firn densification models are very skillful at
842 simulating observed present-day firn density, Δage and $\delta^{15}\text{N}$ over a wide range of climatic conditions.
843 Despite efforts, nobody has been able to satisfactorily remove these inconsistencies via changes to
844 densification physics (Section S2.5).

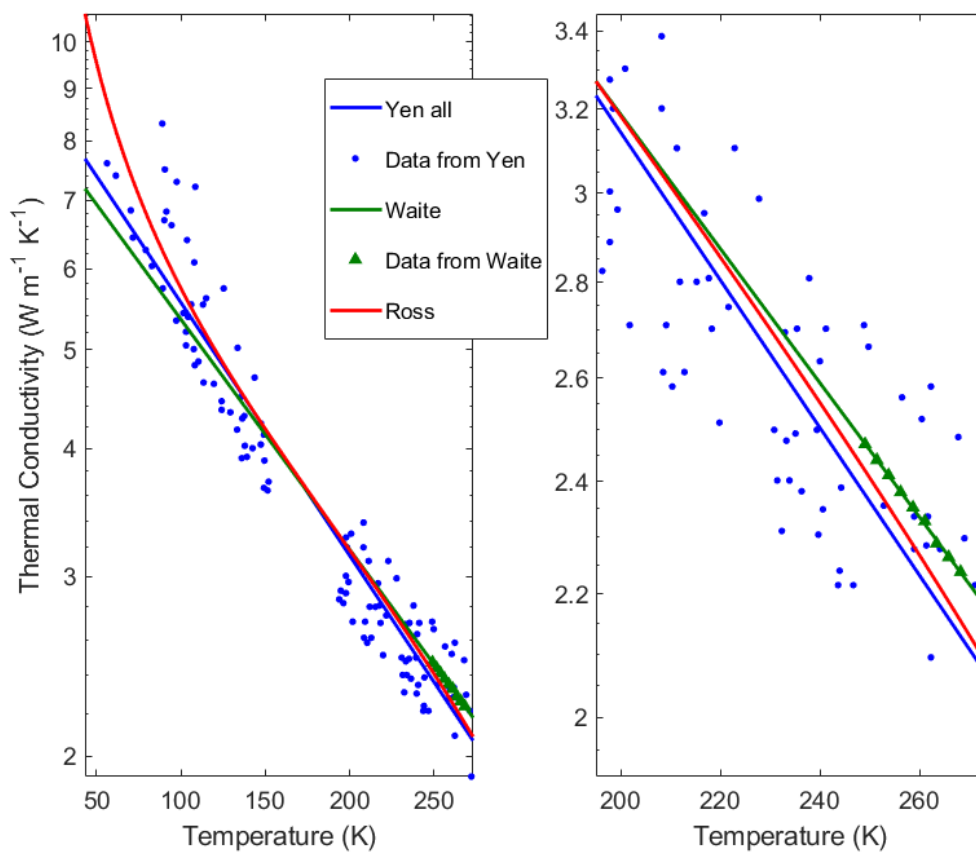
845 For these reasons, we believe that our solution of reduced ΔT_S in central East Antarctica is the most
846 parsimonious solution: it is consistent with the largest amount of observational and model-based evidence,
847 while requiring the fewest number of assumptions. Following the principle of Occam's razor, this means
848 that a small ΔT_S in central East Antarctica should be the preferred scientific hypothesis.

849

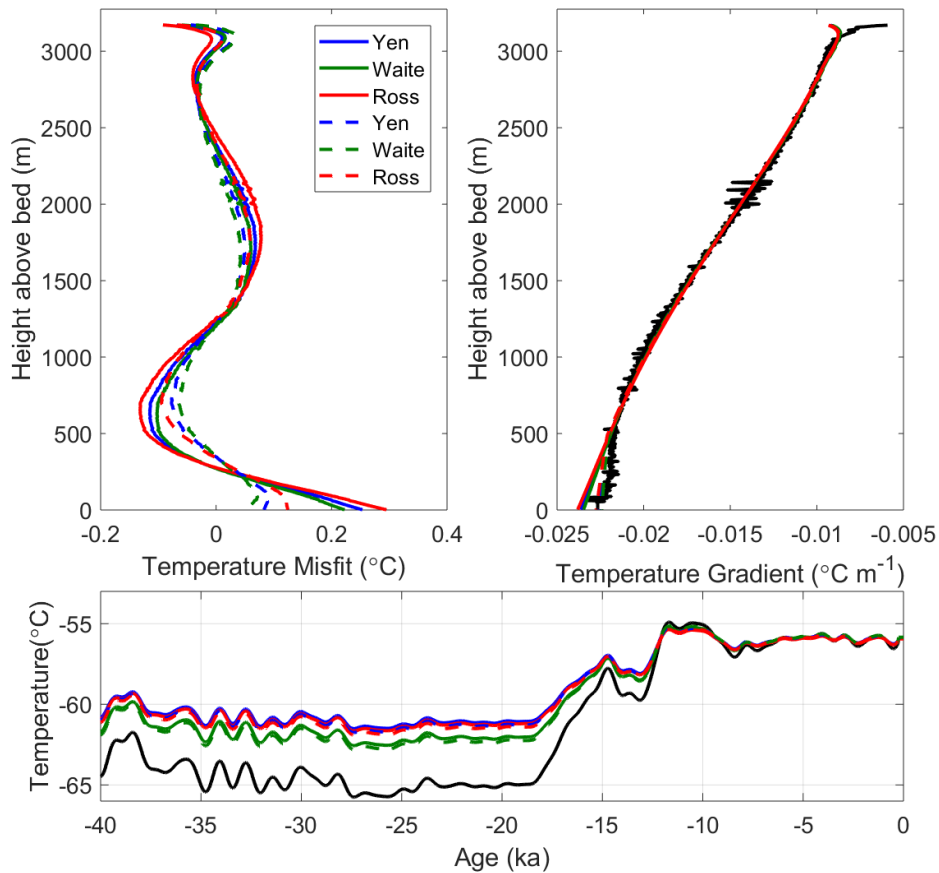


850

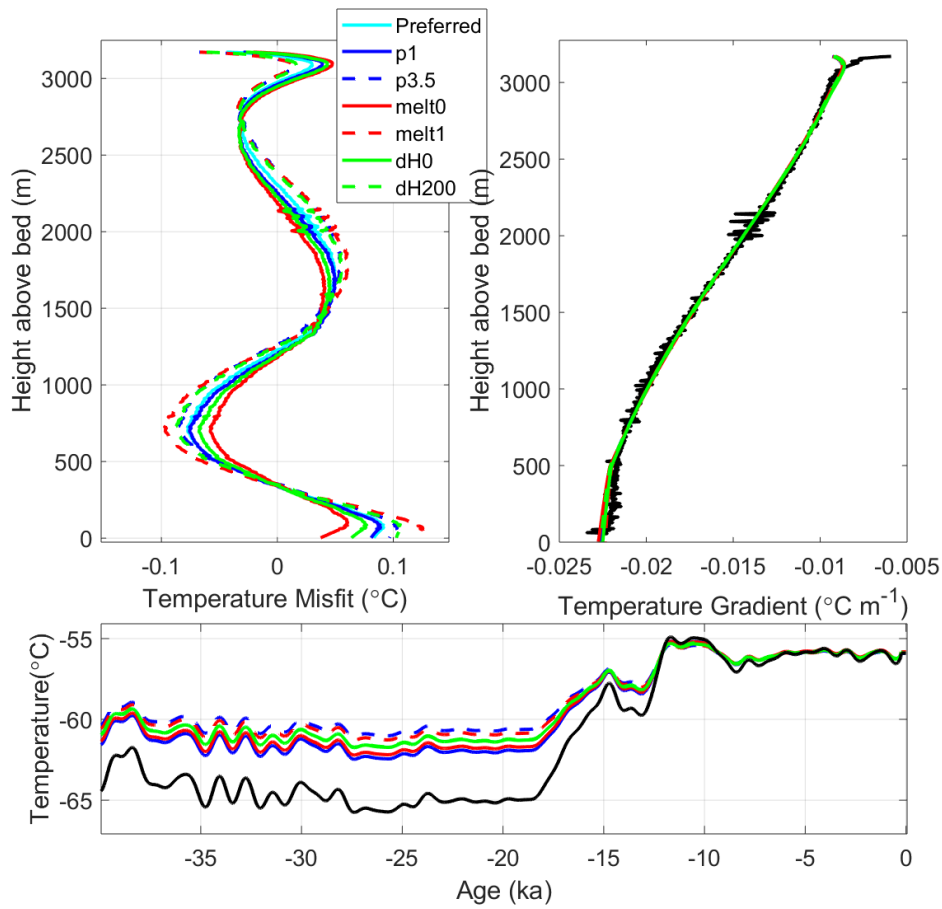
851 **Figure S1: Dome C vertical ice velocity in measurements and models.** Example fit for ApRES data with
 852 Lliboutry approximation where p and w_s are free parameters. This fit has the ApRES measurements shifted
 853 by the mean velocity at depths greater than 3000 m and no basal melt rate applied to the modeled profile.
 854 Table S1 provides the fitted values for other combinations of parameters.



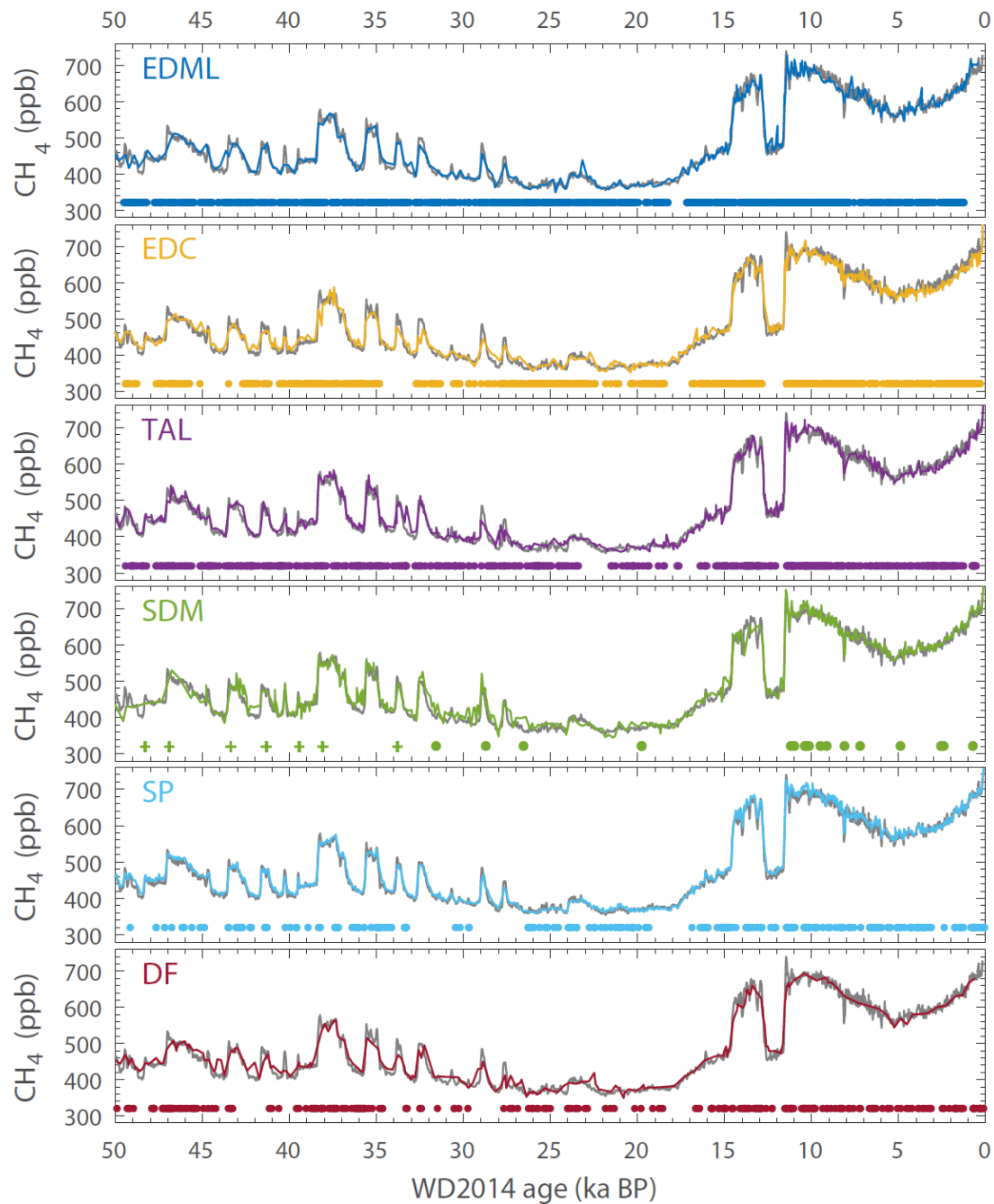
855
 856 **Figure S2: Ice thermal conductivity.** Different relationships for the temperature dependence of thermal
 857 conductivity. “Yen all” refers to the fit using all temperature data from Yen (1981) which is also in Cuffey
 858 and Paterson, 2010 (33, 34). “Waite” refers to our fit to the data in Waite et al., 2006 (45). “Ross” refers to
 859 the fit in Ross et al., 1978 in Table IIIb (44). The left panel shows the full range of the data; the right panel
 860 shows the same focused on the temperature range relevant to the Dome C ice core.



861
 862 **Figure S3: Fitting the Dome C borehole data – sensitivity to thermal conductivity.** Upper left panel:
 863 Measured minus modeled temperature. Upper right panel: Modeled and measured (black) temperature
 864 gradients. Lower panel: Inferred temperature history and temperature history from classical water isotope
 865 scaling (black). The solid lines use the thermal conductivity parameterizations from the respective studies
 866 (legend in top left panel); the dashed shows the same with a 5% thermal conductivity adjustment applied
 867 to the deepest ice as a way to account for the reduced temperature gradient at these depths (top right).

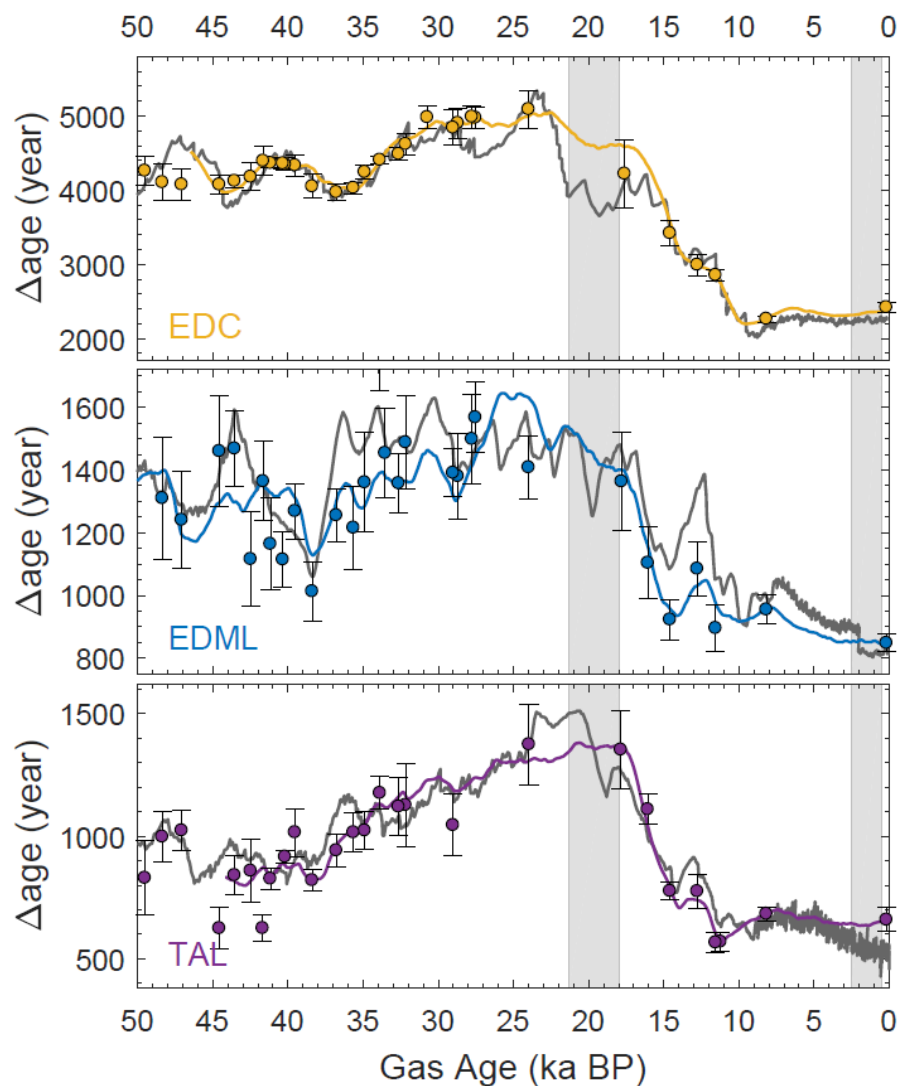


868
 869 **Figure S4: Fitting the Dome C borehole data – sensitivity to ice flow model.** Upper left panel: Measured
 870 minus modeled temperature. Upper right panel: Modeled and measured (black) temperature gradients.
 871 Lower panel: Inferred temperature history and temperature history from classical water isotope scaling
 872 (black). Legend is given in the upper left panel, with descriptions given in the text (Section S).



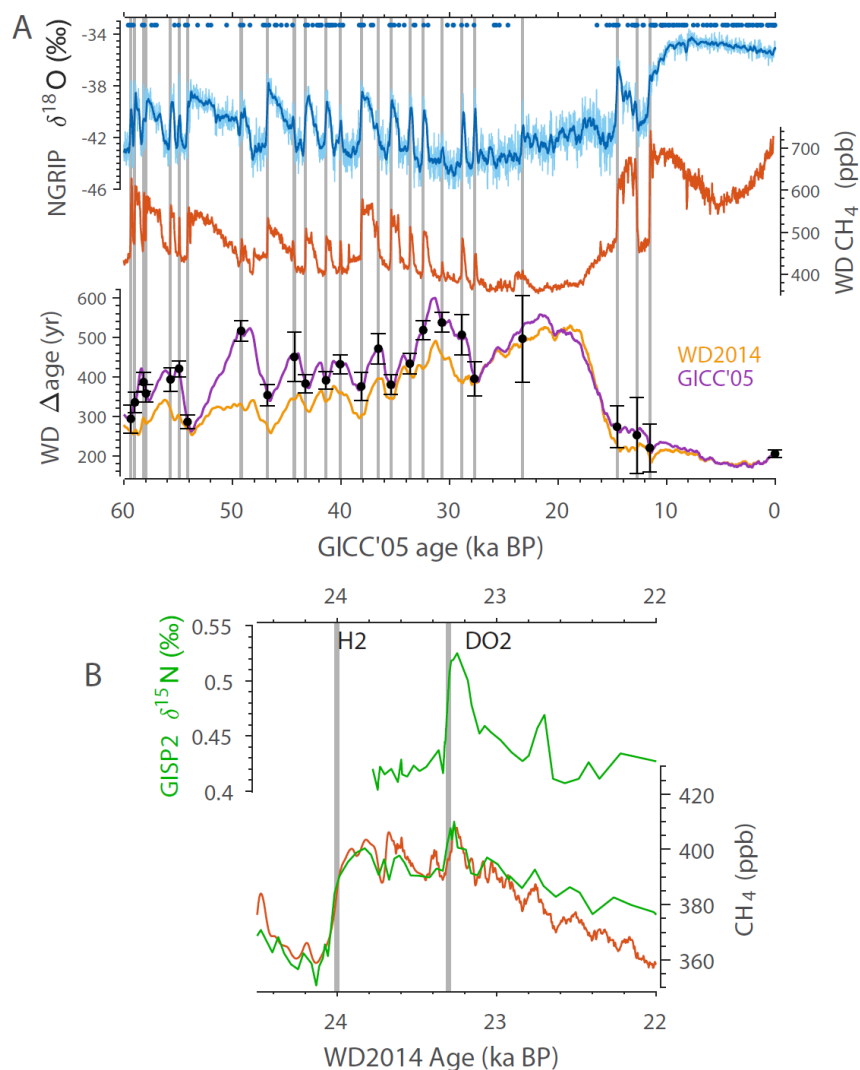
873

874 **Figure S5: Ice core synchronization via atmospheric methane and volcanic markers.** Ice core CH₄ in
 875 the various cores (57, 60, 64-68, 148) as labeled (colored curve) synchronized to the high-resolution WD
 876 CH₄ record (grey curve) on the WD2014 chronology (30, 31, 80). Dots represent the ages of volcanic tie
 877 points, the + symbols (SDM only) represent ice-ice links based on features matched in the $\delta^{18}\text{O}_{\text{ice}}$ records.



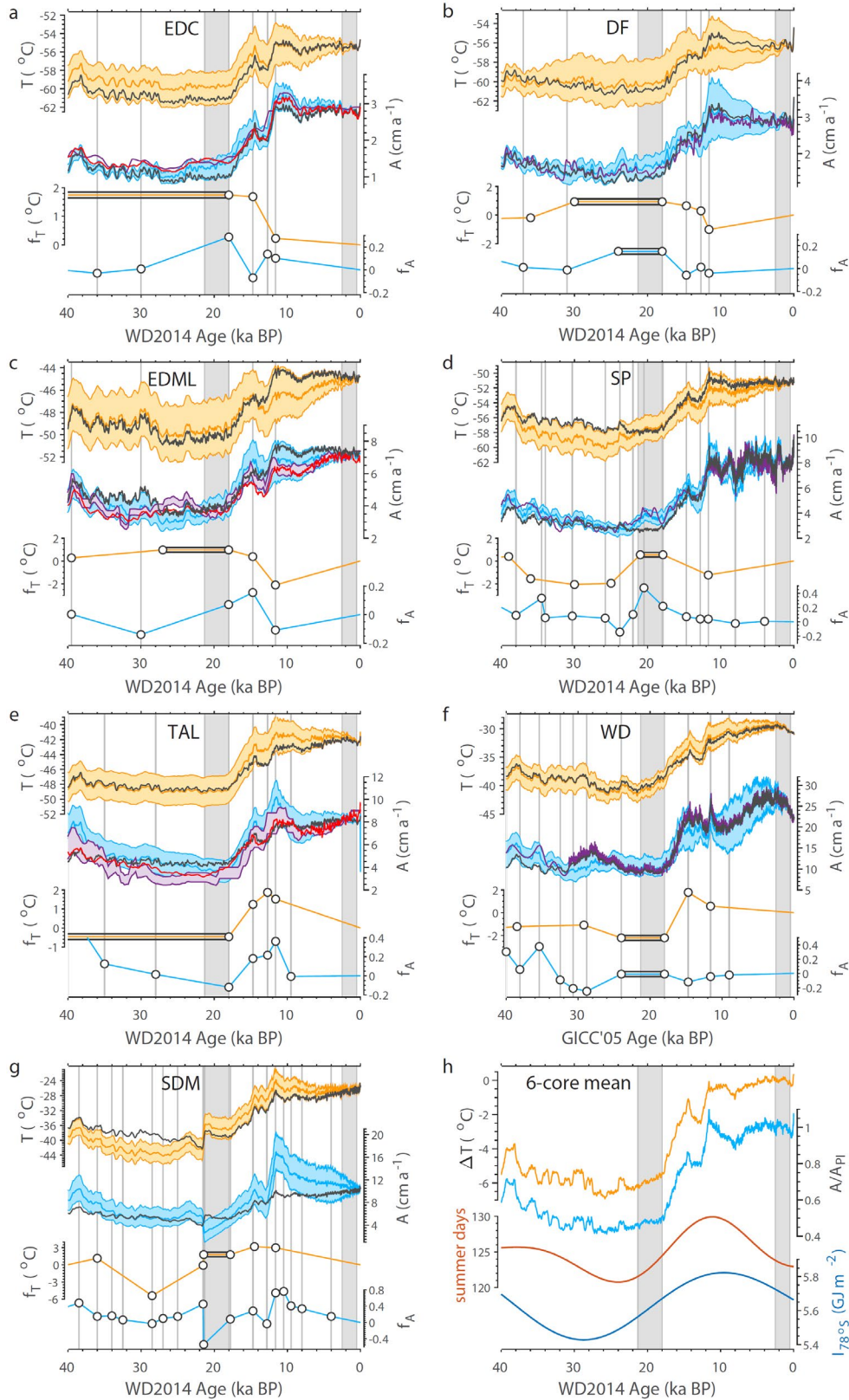
879

880 **Figure S6: Comparison of Δ age to AICC2012.** Empirical Δ age constraints derived here (dots) together
 881 with Δ age from firm densification modeling (colored curve) and Δ age from the AICC2012 Antarctic Ice
 882 Core Chronology (grey curve) for EDC, EDML and TAL (42). Note that in the AICC2012 approach Δ age
 883 is not explicitly modeled; consequently it has abrupt variations (including age inversions) that are likely to
 884 be unphysical. The other four sites considered here (WD, SDM, SP and DF) are not part of the AICC2012
 885 framework. Vertical grey shading denotes the LGM and PI periods.



886

887 **Figure S7: WAIS Divide Δage via bipolar volcanic and CH_4 synchronization.** (a) Greenland NGRIP
 888 $\delta^{18}\text{O}$ as a proxy for climate (upper, blue), with the location of bipolar volcanic tie points given as dots; WD
 889 atmospheric CH_4 (middle, orange); WD Δ age on the WD2014 (30) and GICC'05 timescales (bottom, color
 890 coded as shown). Black dots with errorbars give the empirical (GICC'05-compatible) WD Δ age estimates
 891 based on the inter-polar synchronization. (b) Synchronization at DO2. Top panel: Greenland GISP2 $\delta^{15}\text{N}$
 892 (green); Bottom panel: GISP2 CH_4 (green) and WD CH_4 (orange) data. Greenland warming at DO-2 is
 893 indicated by GISP2 $\delta^{15}\text{N}$, a gas-phase proxy for abrupt Greenland warming (149). Greenland DO-2
 894 warming is coincident with a small ~ 15 ppb CH_4 feature in the GISP2 ice core – the same feature is visible
 895 in the WD core. This allows us to assign a GICC'05 gas age to the WD DO2 CH_4 feature, using the DO-2
 896 GICC'05 ice age. While the Heinrich H-2 CH_4 feature is more pronounced than the DO-2 CH_4 feature, it
 897 cannot be used to synchronize WD to the GICC'05 ice chronology because the H-events are not recorded
 898 in the Greenland ice phase. The H-2 CH_4 feature is used for synchronizing Antarctic CH_4 records from
 899 various cores, however (Fig. S5).



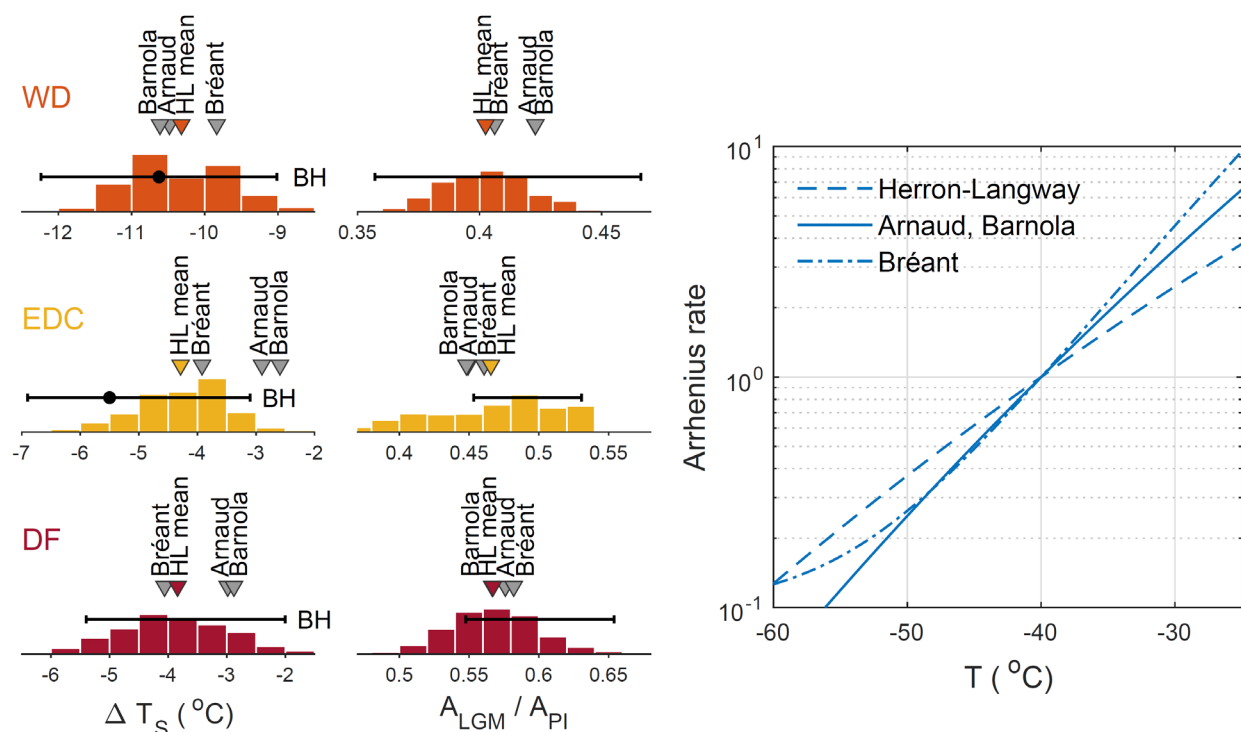
900

901 **Figure S8: Firn-based accumulation rate and temperature reconstructions. (a) EDC; (b) DF; (c)**
 902 **EDML; (d) SP; (e) TAL; (f) WD; (g) SDM. The initial guesses $T_{\text{init}}(t)$ and $A_{\text{init}}(t)$ are shown in grey; the**

903 $T_{\text{site}}(t)$ and $A_{\text{site}}(t)$ reconstructions in orange and blue, respectively, using the Monte Carlo estimation
 904 (Section S2.4) with the envelope giving the 95% confidence range and the center line giving the distribution
 905 mean. The high-frequency T and A variability comes from the $\delta^{18}\text{O}$, not from the optimization method. The
 906 purple curves give accumulation estimates from de-strained layer thickness in the core, the red curves give
 907 the accumulation estimates from the AICC2012 chronology (42). The $f_T(t)$ and $f_A(t)$ modification functions
 908 are shown below in orange and blue, respectively, with the control points and intervals shown as white
 909 circles and grey bars, respectively. (h) Six-core average T and A as anomalies relative to the PI. SDM is
 910 withheld from the averaging because the abrupt 21ka feature is likely a local glaciological effect, and not
 911 representative of Antarctic climate. Summer duration (red, days with insolation over 250 Wm^{-2}) and
 912 annually integrated insolation (blue) are both at 78°S (mean core latitude).

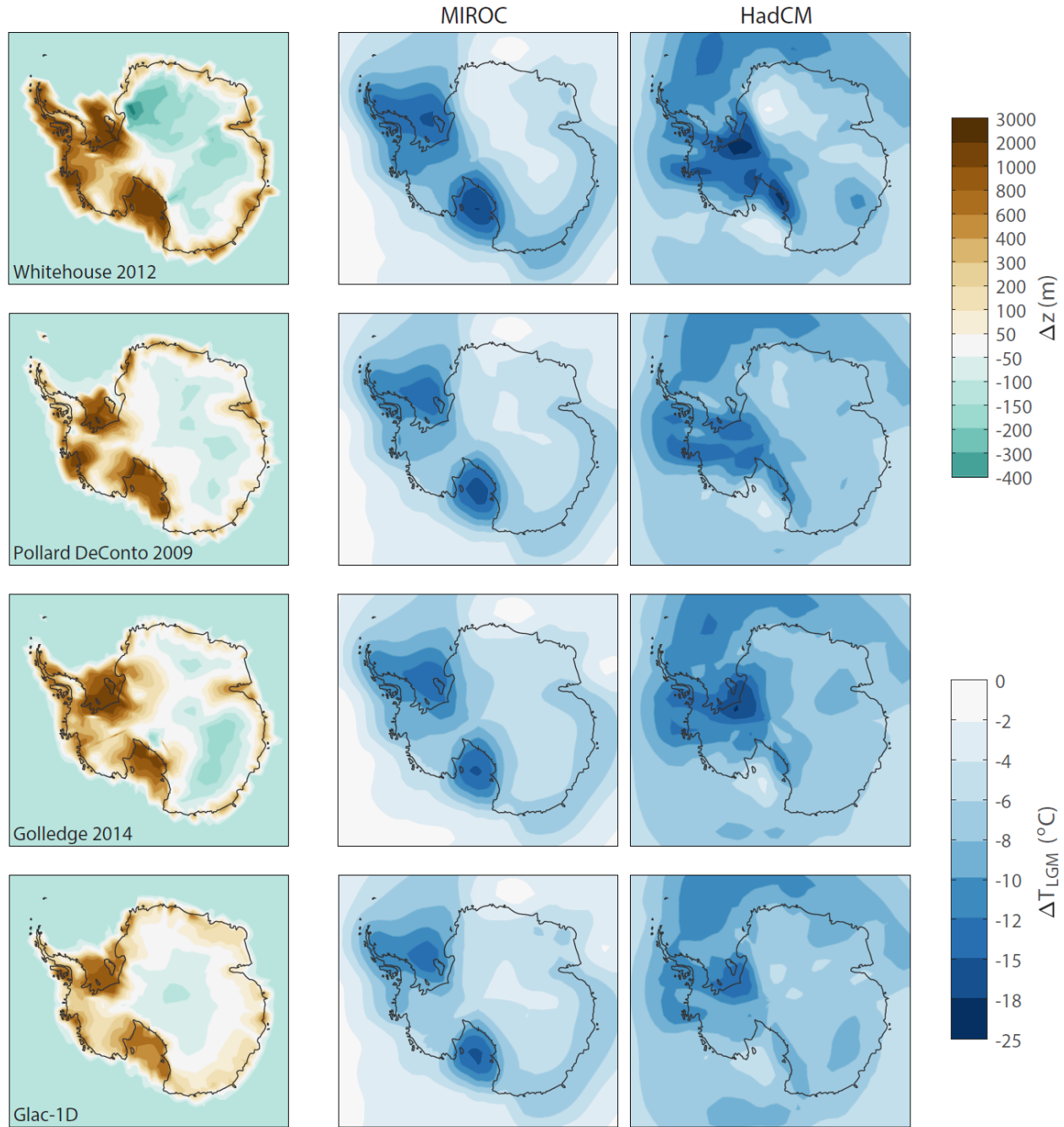
913

914



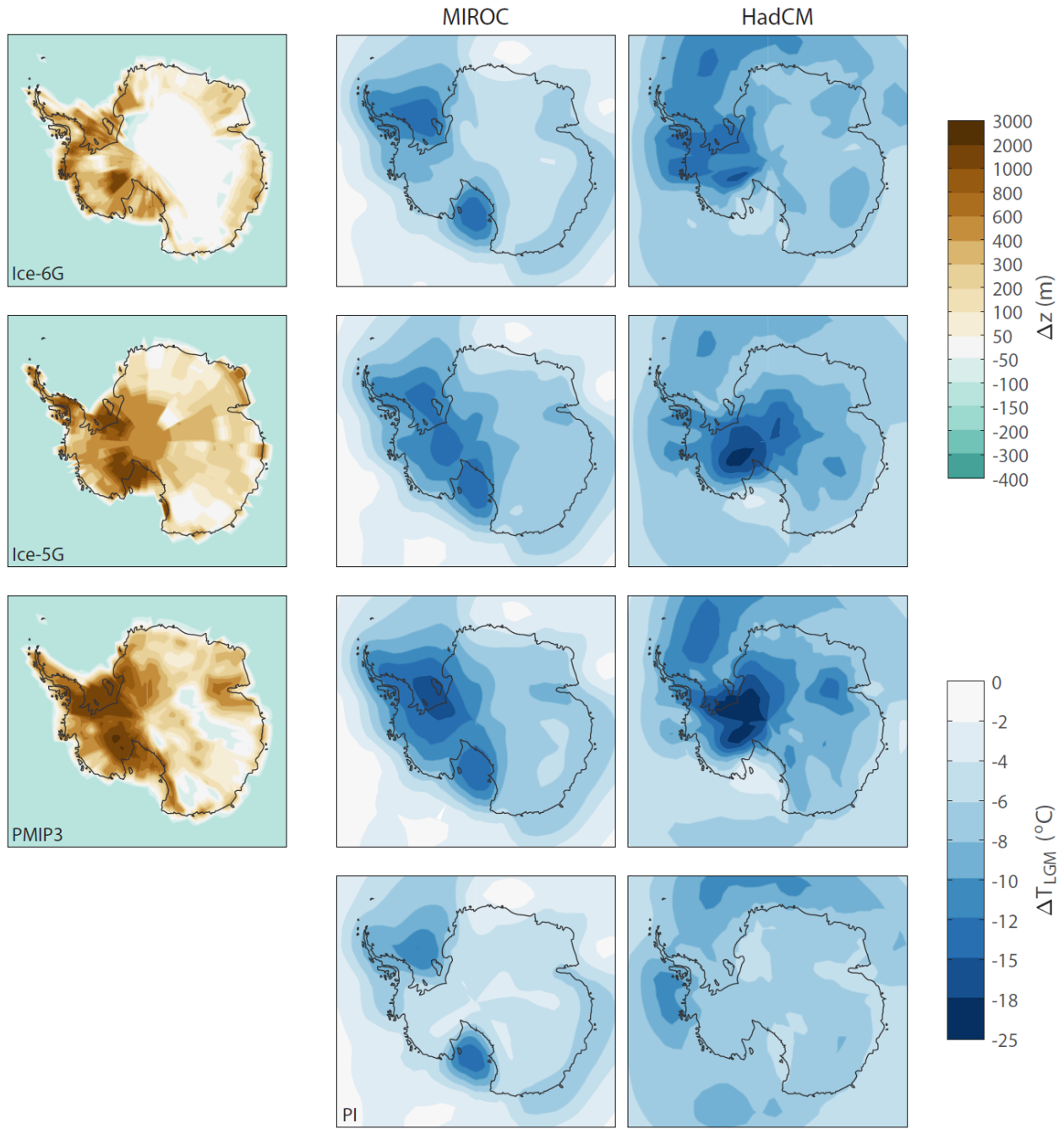
915

916 **Fig. S9. Firn-based climate reconstructions – a model comparison.** Histograms: ice core temperature
 917 and accumulation reconstructions for the WD, EDC and DF sites. Histograms give the spread in the Herron-
 918 Langway Monte Carlo sensitivity study (distribution mean indicated with colored triangles). Results from
 919 the Arnaud (88, 103), Barnola (20, 87) and Bréant (89) firn densification models are indicated by the grey
 920 triangles as marked. Black data and horizontal error bars give the range of borehole temperatures (marked
 921 BH), and the range of accumulation rates consistent with the ice flow model uncertainty used in the borehole
 922 temperature reconstructions. Right panel: plots of the Arrhenius-type activation energy term for the second
 923 stage of firn densification in the firn models. The Arrhenius term has the form $\exp(-Q/RT)$, with R the gas
 924 constant, T the Kelvin temperature and Q the activation energy; the Herron-Langway model uses $Q_{\text{HL}} =$
 925 42.6 kJ/mol ; the Arnaud and Barnola models use $Q_A = Q_B = 60 \text{ kJ/mol}$; the Bréant model uses a weighted
 926 sum of three activation energies ($Q_1 = 110 \text{ kJ/mol}$, $Q_2 = 75 \text{ kJ/mol}$, $Q_3 = 1.5 \text{ kJ/mol}$). All values are
 927 normalized to unit Arrhenius rate at -40°C .



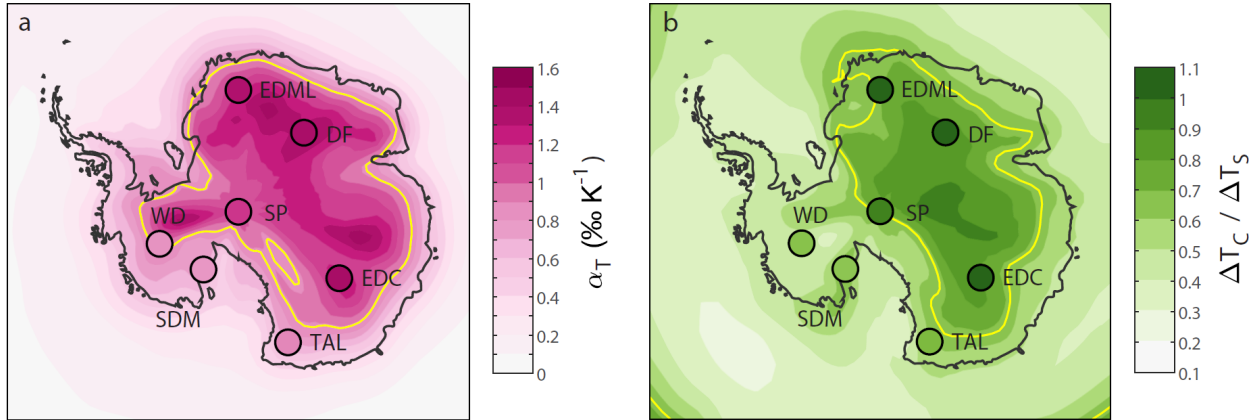
928

929 **Fig S10: Climate model ice sheet sensitivity study (continued on next page).** Left panels: Antarctic
 930 LGM-PI surface topography anomalies used to force the climate model simulations. Topographies as
 931 indicated from refs (29, 50, 116, 121-125). Note that the anomalies are shown relative to the modern geoid,
 932 and as such the LGM sea level drop appears as a negative height anomaly over the oceans. Middle and right
 933 panels: Antarctic cooling ΔT_s simulated in the MIROC and HadCM AOGCMs, respectively, using the
 934 topographic forcing shown in the left panels. The upper five topographies are used in the analyses of the
 935 main manuscript; the Ice-5G and PMIP3 topographies are shown here for comparison purposes.



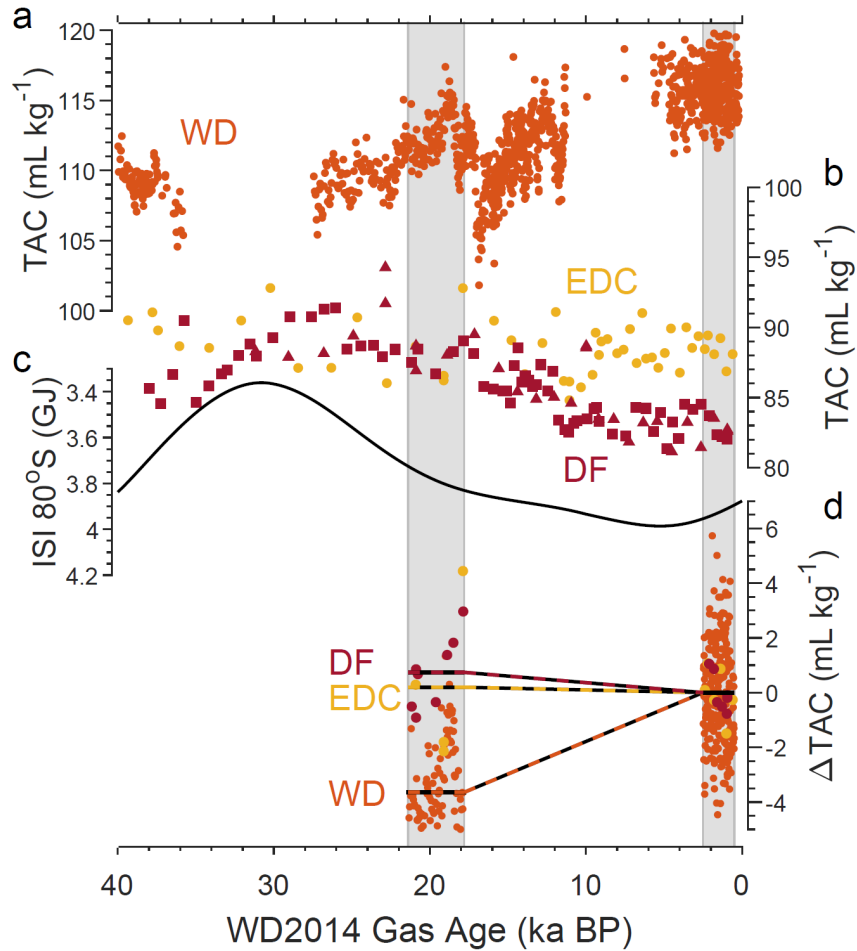
936

937 **Fig. S10 (continued).** Bottom row shows the Pre-industrial ice sheet forcing.



938

939 **Fig S11: Changes to the inversion strength.** (a) Map of the LGM-preindustrial temporal isotope slope in
 940 isotope-enabled CESM simulations (shading), with the same based on the reconstructed ΔT_S (dots). Data
 941 and simulations are corrected for mean-ocean $\delta^{18}\text{O}$. The yellow contour line traces the modern spatial slope
 942 value of 0.8 ‰ K^{-1} (2). (b) Map of the ratio $\Delta T_C / \Delta T_S$ (both calculated as the LGM-preindustrial change)
 943 in the CESM simulations (shading), with the same based on the data-based reconstructions (dots). The 500
 944 hPa temperature is used as a proxy for T_C in CESM; this is the height with the warmest tropospheric
 945 temperatures over interior Antarctica. The yellow contour line follows the modern spatial value 0.65 (2).



946

947 **Fig S12: Total air content records and site elevation change. (a)** WAIS Divide total air content data
 948 (orange). **(b)** EPICA Dome C total air content data (yellow) and Dome Fuji total air content data from the
 949 STAN setup (red triangles) and gas chromatography setup (red squares). **(c)** Integrated summer insolation
 950 at 80°S, a key control on ice core air content (22). **(d)** LGM-PI changes in TAC at the three sites, with DF
 951 and EDC showing a decrease in TAC, and WD showing an increase in TAC through time. These changes
 952 can be interpreted in terms of relative surface elevation change (see text). All air content data are reported
 953 in mL air (at standard temperature and pressure) per kg of ice.

954

955 **Table S1: Fitting the Liboutry equation to the ApRES data.** Fit uses Equation S2 where w_s is the
 956 surface vertical velocity which is the sum of accumulation rate and ice thickness change. The ApRES data
 957 are shown in Fig. S1.

ApRES uniform adjustment (m a ⁻¹)	melt rate in model fit (m a ⁻¹)	p	w_s (m a ⁻¹)
0	0	3.2	0.032
0	-0.0005	2.85	0.032
0	-0.0022	1.2	0.033
0.0022	0	1.7	0.030
0.0015 (0.0022 to 0.0005)	-0.0005	1.35	0.031
	Average	2.06	0.032

958

959

960 **Table S2: The effect of thermal conductivity on reconstructed ΔT_s at EDC.** We find the temperature
 961 history (and ΔT_s) that provides the best fit to the EDC borehole data using three different parameterizations
 962 of thermal conductivity. We either applied no adjustment to basal thermal conductivities, or up to 5%
 963 increased conductivities (as marked). See Section S1.2.1 for more information. All scenarios use our best
 964 estimate ice flow model.

	No Basal Adjustment		Basal Adjustment up to 5%	
	ΔT_s (°C)	RMS (°C)	ΔT_s (°C)	RMS (°C)
Yen (1981)	-5.04	0.0707	-5.29	0.0431
Waite (2006)	-6.01	0.0627	-6.27	0.0359
Ross (1978)	-5.14	0.0817	-5.39	0.0533
Average (all 6)	-5.52			
Range (all 6)	1.23			

965

966

967 **Table S4: Uncertainty estimation for EDC borehole reconstruction.**

p value	2	4	4	4	7	7	7	15	15	15
onset (ka)	none	10	6	2	10	6	2	10	6	2
ΔT_s (°C)	-5.29	-4.85	-4.73	-4.52	-4.51	-4.27	-3.91	-4.14	-3.80	-3.27
ΔT_s change		0.44	0.56	0.77	0.78	1.02	1.38	1.15	1.49	2.02
RMS	.0431	.0468	.0481	.0496	.0505	.0539	.0598	.0553	.0623	.0762
RMS change		.0037	.0050	.0065	.0074	.0108	.0167	.0122	.0192	.0331
Average ΔT_s change		1.07°C								
Range ΔT_s change		2.02°C								

968

969

970 **Table S4: Uncertainty estimation for EDC borehole reconstruction.** The values given represent the uni-
 971 directional uncertainty; the full uncertainty range (interpreted as a 95% confidence interval) equals twice
 972 the values listed. The full ΔT_s uncertainty range stated in the manuscript equals 3.1 to 6.9°C, or $5.0 \pm 1.9^\circ\text{C}$.

	ΔT_s uncertainty $\sigma(\Delta T_s)$
Vertical velocity profile (p)	0.68
Basal melt rate	0.37
Ice thickness history	0.10
Time-variable vertical profile (p)	1.01
Ice flow Total	1.3
Thermal conductivity (Table S2)	0.6
Total Uncertainty (Flow + thermal)	1.9

974

975

976 **Table S5: Firn densification model input parameters and ranges.** Preferred model input parameters
 977 used in the dynamical Herron-Langway firn densification model with their range (noted with σ) used in the
 978 Monte Carlo sensitivity study. CZ is the convective zone thickness; ρ_0 the firn surface density; ρ_{diff}
 979 expresses the density difference between the lock-in (r_{LI}) where gases are effectively isolated from the
 980 atmosphere, and the close-off (r_{CO}) which is known from parameterizations (97), such that $\rho_{\text{LI}} = \rho_{\text{CO}} - \rho_{\text{diff}}$; H
 981 is the ice sheet thickness; GHF is the geothermal heat flux – note that the model was not optimized to
 982 reconstruct this parameter and we advise against using it in other applications.

Site	CZ [m]	σ_1 (CZ) [m]	σ_2 (CZ) [m]	ρ_0 [kg m ⁻³]	σ (ρ_0) [kg m ⁻³]	ρ_{diff} [kg m ⁻³]	$\sigma(\rho_{\text{diff}})$ [kg m ⁻³]	GHF [mW m ⁻²]	H [m]	α_{init} [%K ⁻¹]
EAIS										
EDC	0.0 ^a	2.0	5.0	340	50	4.0	4.0	48	3275	1.1
DF	4.0 ^b	2.0	5.0	335	50	3.0	4.0	54	3038	1.2
EDML	2.0 ^c	2.0	5.0	320	50	5.0	4.0	50	2590	1.15
TAL	5.0 ^d	2.0	5.0	320	50	9.0	4.0	62	1620	0.95
SP	6.0 ^e	2.0	5.0	380	50	15	4.0	56	2600	1.1
WAIS										
WD	3.5 ^f	2.0	5.0	420	50	10	4.0	n/a ^g	1000 ^g	0.88
SDM	2.0 ^h	2.0	5.0	340	50	3.5	4.0	72	1004	0.7

983

984

985

986

987

988

989

990

991

^a) See ref. (150)

^b) Lower bound from model fitting in ref. (151)

^c) Based on EDML firn air data (152)

^d) Generic value used owing to lack of data

^e) Firn-based estimates suggest the CZ is around 3 m at SP (153); increased here to fit ice core $\delta^{15}\text{N}$ data

^f) See ref. (154)

^g) Due to the high accumulation rates at WD, the geothermal heat flux does not meaningfully penetrate into the firn column and only the upper 1000m are simulated in accordance with ref. (30).

^h) See ref. (153).

992 **Table S6: Firn densification model input parameters for alternative firn model physics.** Preferred
 993 model input parameters used in the various firn densification models. CZ is the convective zone thickness;
 994 ρ_0 the firn surface density; ρ_{diff} expresses the density difference between the lock-in (r_{LI}) where gases are
 995 effectively isolated from the atmosphere, and the close-off (r_{LI}) which is known from parameterizations
 996 (97), such that $\rho_{\text{LI}} = \rho_{\text{CO}} - \rho_{\text{diff}}$; H, GHF and α_{init} are as in Table S5 and identical for the different models.

Site and Model	CZ [m]	ρ_0 [kg m ⁻³]	ρ_{diff} [kg m ⁻³]
WDC			
Herron-Langway	3.5	420	10
Arnaud	3.5 ^a	390	-2.0
Barnola	3.5 ^a	420	10
Bréant	3.5 ^a	420	6.0
EDC			
Herron-Langway	0.0	340	4.0
Arnaud	1.0 ^b	340	-2.0
Barnola	1.0 ^b	340	4.0
Bréant	1.0 ^b	340	1.0
DF			
Herron-Langway	4.0	335	3.0
Arnaud	4.0	335	-3.0
Barnola	4.0	335	3.0
Bréant	4.0	335	-1.0

997
 998 **Table S7: Relative elevation changes inferred from total air content records.** All elevation changes are
 999 expressed as relative WAIS (WD) minus EAIS (EDC, DF) LGM elevation changes, and not absolute
 1000 changes relative to the geoid. So a value of +400 m could for example indicate a 300 m elevation increase
 1001 at WD, and a 100 m of elevation decrease at EDC/DF, or for example a 500m elevation increase at WD
 1002 and a 100m elevation increase at EDC/DF. See the text (Section S4) for details. The values marked with
 1003 letters C, L, and U, are used as the central estimate, lower bound and upper bound, respectively, reported
 1004 in the main manuscript (in two significant digits).

	Lower bound [m]	Weighted mean [m]	Upper bound [m]
No insolation correction			
WD-EDC	418	496	516
WD-DF	453	563	588 U
mean	436	530	552
Best-estimate insolation correction			
WD-EDC	346	388	429
WD-DF	380	445	496
mean	363	417 C	462
2 × best-estimate insolation correction			
WD-EDC	275 L	278	342
WD-DF	308	325	404
mean	291	302	373

1005 **Supplementary references and notes**

- 1006 32. L. Lliboutry, A critical review of analytical approximate solutions for steady state velocities and
1007 temperatures in cold ice-sheets. *Gletscherkd. Glazialgeol* **15**, 135–148 (1979).
- 1008 33. K. M. Cuffey, W. S. B. Paterson, *The physics of glaciers, 4th edition*. (Butterworth-Heinemann,
1009 Oxford, UK, 2010), pp. 693.
- 1010 34. Y.-C. Yen, *Review of thermal properties of snow, ice, and sea ice*. (US Army, Corps of Engineers,
1011 Cold Regions Research and Engineering Laboratory, 1981), vol. 81.
- 1012 35. N. Calonne *et al.*, Thermal Conductivity of Snow, Firn, and Porous Ice From 3-D Image-Based
1013 Computations. *Geophys. Res. Lett.* **46**, 13079-13089 (2019).
- 1014 36. G. D. Clow, R. W. Saltus, E. D. Waddington, A new high-precision borehole-temperature logging
1015 system used at GISP2, Greenland, and Taylor Dome, Antarctica. *J. Glaciol.* **42**, 576-584 (1996).
- 1016 37. K. W. Nicholls *et al.*, A ground-based radar for measuring vertical strain rates and time-varying
1017 basal melt rates in ice sheets and shelves. *J. Glaciol.* **61**, 1079-1087 (2015).
- 1018 38. J. Kingslake *et al.*, Full-depth englacial vertical ice sheet velocities measured using phase-
1019 sensitive radar. *Journal of Geophysical Research: Earth Surface* **119**, 2014JF003275 (2014).
- 1020 39. F. Parrenin *et al.*, 1-D-ice flow modelling at EPICA Dome C and Dome Fuji, East Antarctica.
1021 (2007).
- 1022 40. C. Buizert *et al.*, Abrupt ice-age shifts in southern westerly winds and Antarctic climate forced
1023 from the north. *Nature* **563**, 681-685 (2018).
- 1024 41. L. Bazin *et al.*, An optimized multi-proxy, multi-site Antarctic ice and gas orbital chronology
1025 (AICC2012): 120–800 ka. *Clim. Past* **9**, 1715-1731 (2013).
- 1026 42. D. Veres *et al.*, The Antarctic ice core chronology (AICC2012): an optimized multi-parameter and
1027 multi-site dating approach for the last 120 thousand years. *Clim. Past* **9**, 1733-1748 (2013).
- 1028 43. R. Uemura *et al.*, Asynchrony between Antarctic temperature and CO2 associated with obliquity
1029 over the past 720,000 years. *Nature Communications* **9**, 961 (2018).
- 1030 44. R. Ross, P. Andersson, G. Bäckström, Effects of H and D order on the thermal conductivity of ice
1031 phases. *The Journal of Chemical Physics* **68**, 3967-3972 (1978).
- 1032 45. W. F. Waite, L. Y. Gilbert, W. J. Winters, D. H. Mason, Estimating thermal diffusivity and specific
1033 heat from needle probe thermal conductivity data. *Review of Scientific Instruments* **77**, 044904
1034 (2006).
- 1035 46. G. Durand *et al.*, in *Physics of Ice Core Records II*, T. Hondoh, Ed. (Institute of Low Temperature
1036 Science, Hokkaido University, 2009), pp. 91-105.
- 1037 47. L. Bonales, A. C. Rodríguez, P. Sanz, Thermal conductivity of ice prepared under different
1038 conditions. *International journal of food properties* **20**, 610-619 (2017).
- 1039 48. C. F. Raymond, Deformation in the vicinity of ice divides. *J. Glaciol.* **29**, 357-373 (1983).
- 1040 49. R. M. DeConto, D. Pollard, Contribution of Antarctica to past and future sea-level rise. *Nature*
1041 **531**, 591-597 (2016).
- 1042 50. N. R. Golledge *et al.*, Antarctic contribution to meltwater pulse 1A from reduced Southern Ocean
1043 overturning. *Nat Commun* **5**, (2014).
- 1044 51. K. Matsuoka *et al.*, Antarctic ice rises and rumples: Their properties and significance for ice-
1045 sheet dynamics and evolution. *Earth-Sci. Rev.* **150**, 724-745 (2015).
- 1046 52. D. Dahl-Jensen *et al.*, Past Temperatures Directly from the Greenland Ice Sheet. *Science* **282**,
1047 268-271 (1998).
- 1048 53. K. Kawamura *et al.*, State dependence of climatic instability over the past 720,000 years from
1049 Antarctic ice cores and climate modeling. *Science Advances* **3**, (2017).

- 1050 54. J. P. Severinghaus, R. Beaudette, M. A. Headly, K. Taylor, E. J. Brook, Oxygen-18 of O₂ Records
1051 the Impact of Abrupt Climate Change on the Terrestrial Biosphere. *Science* **324**, 1431-1434
1052 (2009).
- 1053 55. D. A. Winski *et al.*, The SP19 chronology for the South Pole Ice Core – Part 1: volcanic matching
1054 and annual layer counting. *Clim. Past* **15**, 1793-1808 (2019).
- 1055 56. E. Capron *et al.*, Glacial–interglacial dynamics of Antarctic firn columns: comparison between
1056 simulations and ice core air- $\delta^{15}\text{N}$ measurements. *Clim. Past* **9**, 983-999 (2013).
- 1057 57. K. Kawamura, Tohoku University, Japan, (2000).
- 1058 58. M. A. Headly, University of California San Diego, (2008).
- 1059 59. J. P. Severinghaus, A. Grachev, B. Luz, N. Caillon, A method for precise measurement of argon
1060 40/36 and krypton/argon ratios in trapped air in polar ice with applications to past firn thickness
1061 and abrupt climate change in Greenland and at Siple Dome, Antarctica. *Geochim. Cosmochim.*
1062 *Acta* **67**, 325-343 (2003).
- 1063 60. L. Loulergue *et al.*, Orbital and millennial-scale features of atmospheric CH₄ over the past
1064 800,000 years. *Nature* **453**, 383-386 (2008).
- 1065 61. A. Schilt *et al.*, Glacial-interglacial and millennial-scale variations in the atmospheric nitrous
1066 oxide concentration during the last 800,000 years. *Quat. Sci. Rev.* **In Press, Corrected Proof**,
1067 (2009).
- 1068 62. A. M. Seltzer *et al.*, Does $\delta^{18}\text{O}$ of O₂ record meridional shifts in tropical rainfall? *Clim. Past* **13**,
1069 1323-1338 (2017).
- 1070 63. R. Spahni *et al.*, Atmospheric methane and nitrous oxide of the late Pleistocene from Antarctic
1071 ice cores. *Science* **310**, 1317-1321 (2005).
- 1072 64. E. J. Brook *et al.*, Timing of millennial-scale climate change at Siple Dome, West Antarctica,
1073 during the last glacial period. *Quat. Sci. Rev.* **24**, 1333-1343 (2005).
- 1074 65. J. Ahn, E. J. Brook, Siple Dome ice reveals two modes of millennial CO₂ change during the last ice
1075 age. *Nat Commun* **5**, (2014).
- 1076 66. J. W. Yang, J. Ahn, E. J. Brook, Y. Ryu, Atmospheric methane control mechanisms during the early
1077 Holocene. *Clim. Past* **13**, 1227-1242 (2017).
- 1078 67. J. Ahn, E. J. Brook, C. Buizert, Response of atmospheric CO₂ to the abrupt cooling event
1079 8200 years ago. *Geophys. Res. Lett.* **41**, 604–609 (2014).
- 1080 68. J. Ahn, E. J. Brook, A. Schmittner, K. Kreutz, Abrupt change in atmospheric CO₂ during the last
1081 ice age. *Geophys. Res. Lett.* **39**, L18711 (2012).
- 1082 69. EPICA-Community-Members, One-to-one coupling of glacial climate variability in Greenland and
1083 Antarctica. *Nature* **444**, 195-198 (2006).
- 1084 70. WAIS-Divide-Project-Members, Onset of deglacial warming in West Antarctica driven by local
1085 orbital forcing. *Nature* **500**, 440-444 (2013).
- 1086 71. WAIS-Divide-Project-Members, Precise inter-polar phasing of abrupt climate change during the
1087 last ice age. *Nature* **520**, 661-665 (2015).
- 1088 72. B. Stenni *et al.*, Expression of the bipolar see-saw in Antarctic climate records during the last
1089 deglaciation. *Nat. Geosci.* **4**, 46-49 (2011).
- 1090 73. E. J. Steig *et al.*, South Pole high resolution ice core water stable isotope record for dD, d¹⁸O.
1091 *U.S. Antarctic Program (USAP) Data Center*, (2020).
- 1092 74. E. J. Steig *et al.*, Recent climate and ice-sheet changes in West Antarctica compared with the
1093 past 2,000 years. *Nature Geosci* **6**, 372-375 (2013).
- 1094 75. B. R. Markle *et al.*, Global atmospheric teleconnections during Dansgaard-Oeschger events.
1095 *Nature Geosci* **10**, 36-40 (2017).
- 1096 76. C. Waelbroeck *et al.*, Sea-level and deep water temperature changes derived from benthic
1097 foraminifera isotopic records. *Quat. Sci. Rev.* **21**, 295-305 (2002).

- 1098 77. T. J. Fudge, K. C. Taylor, E. D. Waddington, J. J. Fitzpatrick, H. Conway, Electrical stratigraphy of
1099 the WAIS Divide ice core: Identification of centimeter-scale irregular layering. *Journal of*
1100 *Geophysical Research: Earth Surface* **121**, 2016JF003845 (2016).
- 1101 78. N. W. Dunbar, A. V. Kurbatov, Tephrochronology of the Siple Dome ice core, West Antarctica:
1102 correlations and sources. *Quat. Sci. Rev.* **30**, 1602-1614 (2011).
- 1103 79. N. W. Dunbar *et al.*, New Zealand supereruption provides time marker for the Last Glacial
1104 Maximum in Antarctica. *Scientific Reports* **7**, 12238 (2017).
- 1105 80. R. H. Rhodes *et al.*, Enhanced tropical methane production in response to iceberg discharge in
1106 the North Atlantic. *Science* **348**, 1016-1019 (2015).
- 1107 81. S. Fujita, F. Parrenin, M. Severi, H. Motoyama, E. W. Wolff, Volcanic synchronization of Dome
1108 Fuji and Dome C Antarctic deep ice cores over the past 216 kyr. *Clim. Past* **11**, 1395-1416 (2015).
- 1109 82. M. Severi *et al.*, Synchronisation of the EDML and EDC ice cores for the last 52 kyr by volcanic
1110 signature matching. *Clim. Past* **3**, 367-374 (2007).
- 1111 83. M. Severi, R. Udisti, S. Becagli, B. Stenni, R. Traversi, Volcanic synchronisation of the EPICA-DC
1112 and TALDICE ice cores for the last 42 kyr BP. *Clim. Past* **8**, 509-517 (2012).
- 1113 84. A. Svensson *et al.*, Bipolar volcanic synchronization of abrupt climate change in Greenland and
1114 Antarctic ice cores during the last glacial period. *Clim. Past Discuss.* **2020**, 1-28 (2020).
- 1115 85. J. L. Rosen *et al.*, An ice core record of near-synchronous global climate changes at the Bolling
1116 transition. *Nat. Geosci.* **7**, 459-463 (2014).
- 1117 86. M. Baumgartner *et al.*, NGRIP CH₄ concentration from 120 to 10 kyr before present and its
1118 relation to a $\delta^{15}\text{N}$ temperature reconstruction from the same ice core. *Clim. Past* **10**, 903-920
1119 (2014).
- 1120 87. J. M. Barnola, P. Pimienta, D. Raynaud, Y. S. Korotkevich, CO₂-climate relationship as deduced
1121 from the Vostok ice core: a re-examination based on new measurements and on a re-evaluation
1122 of the air dating. *Tellus* **43**, 83-90 (1991).
- 1123 88. C. Goujon, J. M. Barnola, C. Ritz, Modeling the densification of polar firn including heat diffusion:
1124 Application to close-off characteristics and gas isotopic fractionation for Antarctica and
1125 Greenland sites. *J. Geophys. Res.* **108**, 18 (2003).
- 1126 89. C. Bréant, P. Martinerie, A. Orsi, L. Arnaud, A. Landais, Modelling firn thickness evolution during
1127 the last deglaciation: constraints on sensitivity to temperature and impurities. *Clim. Past* **13**,
1128 833-853 (2017).
- 1129 90. P. Kindler *et al.*, Temperature reconstruction from 10 to 120 kyr b2k from the NGRIP ice core.
1130 *Clim. Past* **10**, 887-902 (2014).
- 1131 91. C. Huber *et al.*, Isotope calibrated Greenland temperature record over Marine Isotope Stage 3
1132 and its relation to CH₄. *Earth Planet. Sci. Lett.* **243**, 504-519 (2006).
- 1133 92. J. Schwander, B. Stauffer, AGE DIFFERENCE BETWEEN POLAR ICE AND THE AIR TRAPPED IN ITS
1134 BUBBLES. *Nature* **311**, 45-47 (1984).
- 1135 93. S. O. Rasmussen *et al.*, A first chronology for the North Greenland Eemian Ice Drilling (NEEM) ice
1136 core. *Clim. Past* **9**, 2713-2730 (2013).
- 1137 94. I. Seierstad *et al.*, Consistently dated records from the Greenland GRIP, GISP2 and NGRIP ice
1138 cores for the past 104 ka reveal regional millennial-scale isotope gradients with possible
1139 Heinrich Event imprint. *Quat. Sci. Rev.* **106**, 29-46 (2014).
- 1140 95. D. Lilien, A. *et al.*, Holocene Ice-Flow Speedup in the Vicinity of the South Pole. *Geophys. Res.*
1141 *Lett.* **45**, 6557-6565 (2018).
- 1142 96. T. Blunier, J. Schwander, in *Physics of Ice Core Records*, T. Hondoh, Ed. (Hokkaido University
1143 Press, Sapporo, 2000), pp. 307-326.
- 1144 97. P. Martinerie *et al.*, Air content paleo record in the Vostok ice core (Antarctica): A mixed record
1145 of climatic and glaciological parameters. *J. Geophys. Res.* **99**, 10565-10576 (1994).

- 1146 98. E. Witrant *et al.*, A new multi-gas constrained model of trace gas non-homogeneous transport in
1147 firn: evaluation and behaviour at eleven polar sites. *Atmos. Chem. Phys.* **12**, 11465-11483
1148 (2012).
- 1149 99. M. W. Hörhold *et al.*, On the impact of impurities on the densification of polar firn. *Earth Planet.*
1150 *Sci. Lett.* **325–326**, 93-99 (2012).
- 1151 100. J. Freitag, J. Kipfstuhl, T. Laepple, F. Wilhelms, Impurity-controlled densification: a new model
1152 for stratified polar firn. *J. Glaciol.* **59**, 1163-1169 (2013).
- 1153 101. S. FUJITA *et al.*, Densification of layered firn in the ice sheet at Dome Fuji, Antarctica. *J. Glaciol.*
1154 **FirstView**, 1-21 (2016).
- 1155 102. S. Fujita *et al.*, Densification of layered firn of the ice sheet at NEEM, Greenland. *J. Glaciol.* **60**,
1156 905 (2014).
- 1157 103. L. Arnaud, J. M. Barnola, P. Duval, in *Physics of Ice Core Records*, T. Hondoh, Ed. (2000), pp. 285-
1158 305.
- 1159 104. F. Parrenin *et al.*, On the gas-ice depth difference (Δ depth) along the EPICA Dome C ice
1160 core. *Clim. Past* **8**, 1239-1255 (2012).
- 1161 105. A. Landais *et al.*, Firn-air Δ N-15 in modern polar sites and glacial-interglacial ice: a model-
1162 data mismatch during glacial periods in Antarctica? *Quat. Sci. Rev.* **25**, 49-62 (2006).
- 1163 106. G. B. Dreyfus *et al.*, Firn processes and Δ 15N: potential for a gas-phase climate proxy. *Quat.*
1164 *Sci. Rev.* **29**, 28-42 (2010).
- 1165 107. M. Guillevic *et al.*, Spatial gradients of temperature, accumulation and Δ 18O-ice in
1166 Greenland over a series of Dansgaard-Oeschger events. *Clim. Past* **9**, 1029-1051 (2013).
- 1167 108. J. P. Severinghaus *et al.*, Deep air convection in the firn at a zero-accumulation site, central
1168 Antarctica. *Earth Planet. Sci. Lett.* **293**, 359-367 (2010).
- 1169 109. C. Gordon *et al.*, The simulation of SST, sea ice extents and ocean heat transports in a version of
1170 the Hadley Centre coupled model without flux adjustments. *Clim. Dyn.* **16**, 147-168 (2000).
- 1171 110. P. J. Valdes *et al.*, The BRIDGE HadCM3 family of climate models: HadCM3@ Bristol v1. 0.
1172 *Geoscientific Model Development* **10**, 3715-3743 (2017).
- 1173 111. P. Braconnot *et al.*, Results of PMIP2 coupled simulations of the Mid-Holocene and Last Glacial
1174 Maximum - Part 2: feedbacks with emphasis on the location of the ITCZ and mid- and high
1175 latitudes heat budget. *Clim. Past* **3**, 279-296 (2007).
- 1176 112. T. R. Jones *et al.*, Southern Hemisphere climate variability forced by Northern Hemisphere ice-
1177 sheet topography. *Nature* **554**, 351 (2018).
- 1178 113. J. S. Singarayer, P. J. Valdes, P. Friedlingstein, S. Nelson, D. J. Beerling, Late Holocene methane
1179 rise caused by orbitally controlled increase in tropical sources. *Nature* **470**, 82-85 (2011).
- 1180 114. C. D. Hewitt, A. J. Broccoli, J. F. Mitchell, R. J. Stouffer, A coupled model study of the last glacial
1181 maximum: Was part of the North Atlantic relatively warm? *Geophys. Res. Lett.* **28**, 1571-1574
1182 (2001).
- 1183 115. P. Braconnot *et al.*, Results of PMIP2 coupled simulations of the Mid-Holocene and Last Glacial
1184 Maximum - Part 1: experiments and large-scale features. *Clim. Past* **3**, 261-277 (2007).
- 1185 116. A. Abe-Ouchi *et al.*, Ice-sheet configuration in the CMIP5/PMIP3 Last Glacial Maximum
1186 experiments. *Geosci. Model Dev.* **8**, 3621-3637 (2015).
- 1187 117. H. Hasumi, S. Emori, K-1 coupled GCM (MIROC) description K-1 Technical Report No 1. *Center for*
1188 *Climate System Research*, (2004).
- 1189 118. T. Obase, A. Abe-Ouchi, Abrupt Bølling-Allerød Warming Simulated under Gradual Forcing of the
1190 Last Deglaciation. *Geophys. Res. Lett.* **46**, 11397-11405 (2019).
- 1191 119. A. Yamamoto *et al.*, Global deep ocean oxygenation by enhanced ventilation in the Southern
1192 Ocean under long-term global warming. *Global Biogeochemical Cycles* **29**, 1801-1815 (2015).

- 1193 120. S. Sherriff-Tadano, A. Abe-Ouchi, Roles of Sea Ice–Surface Wind Feedback in Maintaining the
1194 Glacial Atlantic Meridional Overturning Circulation and Climate. *J. Clim.* **33**, 3001-3018 (2020).
- 1195 121. M. A. Toscano, W. R. Peltier, R. Drummond, ICE-5G and ICE-6G models of postglacial relative
1196 sea-level history applied to the Holocene coral reef record of northeastern St Croix, U.S.V.I.:
1197 investigating the influence of rotational feedback on GIA processes at tropical latitudes. *Quat.*
1198 *Sci. Rev.* **30**, 3032-3042 (2011).
- 1199 122. P. L. Whitehouse, M. J. Bentley, A. M. Le Brocq, A deglacial model for Antarctica: geological
1200 constraints and glaciological modelling as a basis for a new model of Antarctic glacial isostatic
1201 adjustment. *Quat. Sci. Rev.* **32**, 1-24 (2012).
- 1202 123. D. Pollard, R. M. DeConto, Modelling West Antarctic ice sheet growth and collapse through the
1203 past five million years. *Nature* **458**, 329-332 (2009).
- 1204 124. W. Peltier, Global glacial isostasy and the surface of the ice-age Earth: the ICE-5G (VM2) model
1205 and GRACE. *Annu. Rev. Earth Planet. Sci.* **32**, 111-149 (2004).
- 1206 125. W. R. Peltier, D. Argus, R. Drummond, Space geodesy constrains ice age terminal deglaciation:
1207 The global ICE-6G_C (VM5a) model. *Journal of Geophysical Research: Solid Earth* **120**, 450-487
1208 (2015).
- 1209 126. J. W. Hurrell *et al.*, The Community Earth System Model: A Framework for Collaborative
1210 Research. *Bulletin of the American Meteorological Society* **94**, 1339-1360 (2013).
- 1211 127. E. Brady *et al.*, The Connected Isotopic Water Cycle in the Community Earth System Model
1212 Version 1. *Journal of Advances in Modeling Earth Systems* **11**, 2547-2566 (2019).
- 1213 128. E. C. Brady, B. L. Otto-Bliesner, J. E. Kay, N. Rosenbloom, Sensitivity to Glacial Forcing in the
1214 CCSM4. *J. Clim.* **26**, 1901-1925 (2013).
- 1215 129. J. Zhu *et al.*, Reduced ENSO variability at the LGM revealed by an isotope-enabled Earth system
1216 model. *Geophys. Res. Lett.* **44**, 6984-6992 (2017).
- 1217 130. K. E. Kohfeld *et al.*, Southern Hemisphere westerly wind changes during the Last Glacial
1218 Maximum: paleo-data synthesis. *Quat. Sci. Rev.* **68**, 76-95 (2013).
- 1219 131. D. Noone, I. Simmonds, Annular variations in moisture transport mechanisms and the
1220 abundance of $\delta^{18}\text{O}$ in Antarctic snow. *J. Geophys. Res.* **107**, 4742 (2002).
- 1221 132. M. Werner, U. Mikolajewicz, M. Heimann, G. Hoffmann, Borehole versus isotope temperatures
1222 on Greenland: Seasonality does matter. *Geophys. Res. Lett.* **27**, 723-726 (2000).
- 1223 133. G. A. Schmidt, G. Hoffmann, D. T. Shindell, Y. Hu, Modeling atmospheric stable water isotopes
1224 and the potential for constraining cloud processes and stratosphere-troposphere water
1225 exchange. *J. Geophys. Res.* **110**, (2005).
- 1226 134. A. Touzeau *et al.*, Acquisition of isotopic composition for surface snow in East Antarctica and the
1227 links to climatic parameters. *The Cryosphere* **10**, 837-852 (2016).
- 1228 135. J. Guan *et al.*, Understanding the temporal slope of the temperature-water isotope relation
1229 during the deglaciation using isoCAM3: The slope equation. *J. Geophys. Res.* **121**, 2016JD024955
1230 (2016).
- 1231 136. B. Stenni *et al.*, The deuterium excess records of EPICA Dome C and Dronning Maud Land ice
1232 cores (East Antarctica). *Quat. Sci. Rev.* **29**, 146-159 (2010).
- 1233 137. M. Werner, M. Heimann, G. Hoffmann, Isotopic composition and origin of polar precipitation in
1234 present and glacial climate simulations. *Tellus* **53**, 53-71 (2001).
- 1235 138. L. Sime, E. Wolff, K. Oliver, J. Tindall, Evidence for warmer interglacials in East Antarctic ice
1236 cores. *Nature* **462**, 342-345 (2009).
- 1237 139. M. Kageyama *et al.*, The PMIP4-CMIP6 Last Glacial Maximum experiments: preliminary results
1238 and comparison with the PMIP3-CMIP5 simulations. *Clim. Past Discuss.* **2020**, 1-37 (2020).
- 1239 140. V. Lipenkoy, F. Candaudap, J. Ravoire, E. Dulac, D. Raynaud, A new device for the measurement
1240 of air content in polar ice. *J. Glaciol.* **41**, 423-429 (1995).

- 1241 141. S. Sugawara, K. Kawamura, S. Aoki, T. Nakazawa, G. Hashida, Reconstruction of past variations of
1242 delta C-13 in atmospheric CO2 from its vertical distribution observed in the firn at Dome Fuji,
1243 Antarctica. *Tellus* **55**, 159-169 (2003).
- 1244 142. P. Martinerie, V. Y. Lipenkov, D. Raynaud, Correction Of Air-content Measurements In Polar Ice
1245 For The Effect Of Cut Bubbles At The Surface Of The Sample. *J. Glaciol.* **36**, 299-303 (1990).
- 1246 143. L. E. Mitchell *et al.*, Observing and modeling the influence of layering on bubble trapping in polar
1247 firn. *J. Geophys. Res.* **120**, 2014JD022766 (2015).
- 1248 144. D. Raynaud, J. Chappellaz, C. Ritz, P. Martinerie, Air content along the Greenland Ice Core
1249 Project core: A record of surface climatic parameters and elevation in central Greenland. *J.*
1250 *Geophys. Res.-Oceans* **102**, 26607-26613 (1997).
- 1251 145. J. M. Fegyveresi *et al.*, Five millennia of surface temperatures and ice-core bubble characteristics
1252 from the WAIS Divide deep core, West Antarctica. *Paleoceanography*, (2016).
- 1253 146. O. Eicher *et al.*, Climatic and insolation control on the high-resolution total air content in the
1254 NGRIP ice core. *Clim. Past* **12**, 1979-1993 (2016).
- 1255 147. J. O. Stone, Air pressure and cosmogenic isotope production. *J. Geophys. Res.-Solid Earth* **105**,
1256 23753-23759 (2000).
- 1257 148. A. Schilt *et al.*, Atmospheric nitrous oxide during the last 140,000 years. *Earth Planet. Sci. Lett.*
1258 **300**, 33-43 (2010).
- 1259 149. J. P. Severinghaus, T. Sowers, E. J. Brook, R. B. Alley, M. L. Bender, Timing of abrupt climate
1260 change at the end of the Younger Dryas interval from thermally fractionated gases in polar ice.
1261 *Nature* **391**, 141-146 (1998).
- 1262 150. F. Parrenin *et al.*, Synchronous Change of Atmospheric CO2 and Antarctic Temperature During
1263 the Last Deglacial Warming. *Science* **339**, 1060-1063 (2013).
- 1264 151. K. Kawamura *et al.*, Convective mixing of air in firn at four polar sites. *Earth Planet. Sci. Lett.* **244**,
1265 672-682 (2006).
- 1266 152. G. Dreyfus, Princeton University, (2008).
- 1267 153. J. P. Severinghaus, M. O. Battle, Fractionation of gases in polar ice during bubble close-off: New
1268 constraints from firn air Ne, Kr and Xe observations. *Earth Planet. Sci. Lett.* **244**, 474-500 (2006).
- 1269 154. M. O. Battle *et al.*, Controls on the movement and composition of firn air at the West Antarctic
1270 Ice Sheet Divide. *Atmos. Chem. Phys.* **11**, 11007-11021 (2011).
- 1271
- 1272